Master's Thesis

Development of a Two-Dimensional Resonator Design Tool

Leiden University Medical Center

Jason Mensingh

Supervisors:
prof. dr. Andrew Webb*
dr. ir. Bert Jan Kooij†
dr. ir. Rob Remis†

October 30, 2013

* C.J. Gorter Center for High Field MRI, Department of Radiology, University Medical Center, Leiden, The Netherlands.

† Microelectronics Department, Delft University of Technology, Delft, The Netherlands.

Abstract

One of the engineering challenges in high-field MRI is to have a homogeneous distribution of the RF magnetic field inside human tissue. In this project we develop a design tool for a HEM wrist applicator that has the ability to generate a homogeneous magnetic field inside human wrist. By taking into account the dominant RF scattering effects inside the wrist we can design the HEM applicator by applying high permittivity materials in such a way that we can compensate for these scattering effects.

In this research project we start by developing a two-dimensional layered cylindrical model for the wrist. The wrist will be excited by line sources located on the outside of the two-dimensional HEM applicator. For this model we can derive a closed-form analytical solution of the electromagnetic RF field in terms of Bessel functions. This model serves as a canonical problem to investigate how the high permittivity materials in the HEM applicator change the homogeneity of the magnetic field. This two-dimensional model will be implemented in Matlab.

The results of this canonical model will be translated to a HEM applicator of finite dimension. The designed HEM applicator's field distribution will be simulated with the commercial software package CST and compared to the results obtained for the canonical model.

Acknowledgements

I would like to thank all colleges at the C.J. Gorter centre for welcoming me into their research group. The research related discussions about electromagnetism which sometimes almost felt philosophical were always fun and interesting. Also the medical researchers were very helpful in explaining all the medical "stuff" and were always interested in my research projects or curious about the weird equations that were on my computer screen. I would also especially like to thank Andrew Webb and Sebastian Aussenhofer for their guidance and support.

Also Paul de Heer, Joep Wezel and Wyger Brink were always there for me if I needed to discuss my research or needed a soundboard to bounce ideas off, thanks guys. From the TUDelft I would first like to thank my supervisors Rob Remis and Bert Jan Kooij for always being there for me and giving me advice and guidance when I needed it the most. Also a special thanks to all the students from the 21st floor and especially Vasiliki Paraforou, our lengthy discussions were always very helpful. Last but not least I would also like to thank all my other friends and family who supported me through everything and would always let me to at least try to explain the research that I was doing. To my mom, dad and Annelies you are the best, thanks for everything

Jason Mensingh
Leiden, The Netherlands
October 23, 2013

Preface

This thesis is the conclusion of my Electrical Engineering masters program at Delft University of Technology. The work of this thesis was partially carried out at the faculty of Electrical Engineering, Mathematics and Computer Science in Delft and the C J. Gorter Center at the Leids Universitair Medisch Centrum or LUMC for short. The Gorter Center houses an experimental 7 Tesla MRI system that allows us to explore new and exciting areas in medical imaging.

In order to get sharp and detailed images from such a system, it is crucial to transmit an as homogeneously possible magnetic field into the patient. To this end, a lot of research has to be done on determining the field distributions inside different structures and materials. This commonly involves time consuming numerical simulations as for most structures an analytical solution is not available. This thesis project assesses the possibility of designing such an analytical tool for calculating the electromagnetic field distributions inside cylindrically layered structures. The benefits from such a tool – apart from having a reduced simulation time (seconds instead of hours) – is that this will create more insight on how and why certain field distributions exist in a multitude of cylindrical layered objects.

In order to solve this kind of problem a lot of electromagnetic equations are involved. The lectures covering those equations are the worst nightmare of every beginning engineering student. I will never forget the time I attended my first lecture about electromagnetic waves. I realized that my head felt like it was going to explode from al the questions that I had. At the same time I found it very intriguing that electromagnetic waves are all around us but so few people really understood how they work. I would have never guessed that my final thesis work would involve the same physics and mathematics

which I feared so much at the beginning of my academic career. I very much hope that I can continue to keep working in this particular field of study after I receive my masters degree in Electrical Engineering.

Contents

Chapter 1

Introduction

1.1 Problem statement

Constructing a dielectric resonator coil for usage in MRI systems is time consuming and labour intensive. Generally these dielectric structures have a high Q-factor and are designed to resonate at a single frequency. The dielectric structure consists of dielectric materials which have a high relative permittivity ($\varepsilon_r \gg 60$) and possess low electric losses ($\sigma \ll 0.1$ S/m).

The desired resonating frequency is equal to that of the Lamor frequency ($f = \gamma B_0$) which is a linear function of the gyromagnetic ratio (γ) of the nuclei in the volume of interest and the magnitude of the static magnetic background field (B_0). Generally, hydrogen nuclei are studied in clinical MRI scans for which the gyromagnetic ratio is about 42 MHz/T.

The static magnetic field strength commonly used in clinical scans is 3T. The C. J. Gorter Center for High-field MRI also has an MRI system which has a magnetic field strength of 7T. Before physically constructing resonators for such 3T or 7T systems, multiple numerical computer simulations have to be performed to get some insight into the electromagnetic behavior of a dielectric resonator. The major downside of these numerical based simulations is that they either require too much computational resources or they need too much time to complete [1]. In addition, highly resonant structures with a high Q-factor will prolong the needed simulation time if a transient solver is used.

Structures with a high Q-factor are constructed with materials which have low losses at the Lamor frequency.

To reduce the simulation times involved in MRI resonator design, it would be preferable to have a fast calculation tool available that is able to analytically calculate the electromagnetic field distribution inside a highly resonating cylindrical dielectric structure with human tissue inserted in it. A general case for determining the electromagnetic field distributions analytically in cylindrical structures has been described in the books of Chew [2] and Balanis [3]. An analytical solution of a somewhat more practical cylindrical structure has been briefly described in the book of Jin [4]. This analytical method determines the electromagnetic fields in a cylindrical structure with a circular sheet current source. However, the method can handle resonator configurations consisting of two layers only and the layers have to be lossless as well.

1.2 Project goal

In this thesis, we extend the method described by Jin to cylindrical configurations consisting of N layers possibly containing losses. Based on our method, we develop a simulation tool in Matlab that allows us to rapidly calculate the electromagnetic field distributions inside highly resonant cylindrically layered high permittivity low loss dielectric structures. This tool can then be used to study field patterns in a variety of cylindrical resonators. In this way we hope to gain an understanding on how to select the optimal resonator design parameters such as the dimensions of the resonator, the thickness of the different layers, material parameters, and the particular form of the excitation source.

1.3 Thesis outline

The outline of this thesis is as follows:

Chapter 2: The MRI system and its key components

Chapter 2 gives a brief overview of the Magnetic Resonance Imaging system. The key components of an MRI scanner are described and the basic physical principles of those components are discussed as well.

Chapter 3: Basic electromagnetic equations

In Chapter 3 we present the basic equations that govern electromagnetic wave phenomena. The constitutive relations and the boundary conditions are discussed as well.

Chapter 4: EM waves in cylindrical homogeneous media

In Chapter 4 we describe the procedure to obtain the analytical solutions for determining the EM field distributions in a cylindrically layered structure.

Chapter 5: Matlab simulation tool and results

Chapter 5 shows the results of the analytical software tool and demonstrates how the tool can be used in resonator design. A comparison between the results obtained with the software tool and a commercial numerical solver is also presented.

Chapter 6: Discussion and conclusion

The conclusions and recommendations are presented in Chapter 6.

Chapter 2

The MRI System and Its Key Components

2.1 The MRI system and its main magnetic field

Presently, MRI is a widely used medical diagnostic tool as it uses non-ionizing radiation that is much safer than for example X-ray radiation. A magnetic resonance imaging system or MRI system (see Figure 2.1) is a very complex machine which has multiple different subsystems. Discussing all these subsystems is clearly beyond the scope of this thesis. We therefore only consider some main aspects of Magnetic Resonance Imaging.

Figure 2.1: Depiction of an MRI system and patient bed.

The key components in an MRI system include a main magnet, a set of gradient coils, an RF coil, a transmitter, a receiver and a computer. The feature people first notice when they see an MRI system for the first time is the large cylindrical structure. This structure houses the main magnet, gradient coils and for most MRI systems also the RF coils (see Figure 2.2).

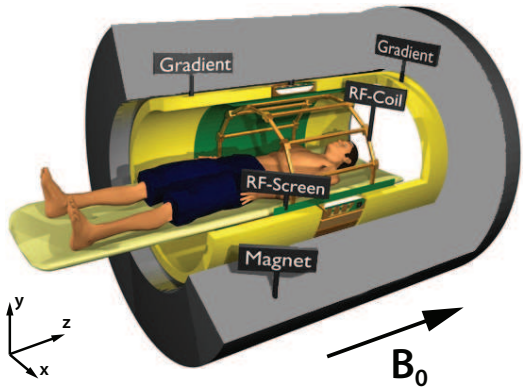

Figure 2.2: Super conducting magnet and its B_0 field orientation.

The main magnet has to generate a strong homogeneous magnetic field called the B_0 field. The B_0 field of clinical 3 Tesla systems is about 50.000 times stronger than that of the Earth's magnetic field. The MRI system uses a superconducting magnet in order to generate such high magnetic field strengths. The magnet is cooled down by liquid Helium to about 4 Kelvin in order to stay superconductive. A stronger main magnetic field will provide a better signal to noise ratio (SNR) and a higher resolution in both the frequency and the spatial domain. The direction of this main magnetic field is commonly considered to be in the "z-direction" of a Cartesian coordinate system.

2.2 RF coils

RF-coils, also called RF-resonators, are key components in an MRI system. In order to obtain high quality MR images, the RF-coils have to satisfy two major requirements.
The first one is to be able to generate a homogeneous magnetic field by transmitting RF-pulses at the Lamor frequency in order to excite the nuclei

inside the volume of interest uniformly. This field called the B_1 field and is perpendicular to the static magnetic field created by the superconducting magnet inside the MR system.
The second requirement is that when used for reception, the RF-coil must have a high signal to noise ratio, also the emitted signals from the nuclei must be received with an equal gain in each point in the volume of interest.

The RF-coils used in MRI scanning systems can be categorized into two groups. The first group consist of "volume antennas" that are used for both transmitting and receiving signals (see Figure 2.3). Examples of such antennas are volume coils and birdcage antennas. These antennas are very popular since in the transmitting state they can produce a very homogeneous B_1 field inside the volume of interest [5]. The second group consist of surface coils like single-loop antennas or surface coil arrays. The surface coils have a high SNR in the receiving state due to the fact that they only pick up noise from a small area compared to that of a volume coil. The surface coils produce a relatively poor homogeneous B_1 field, however, and for this reason they are mainly used for reception only. Two surface coil examples are depicted in Figure 2.4.

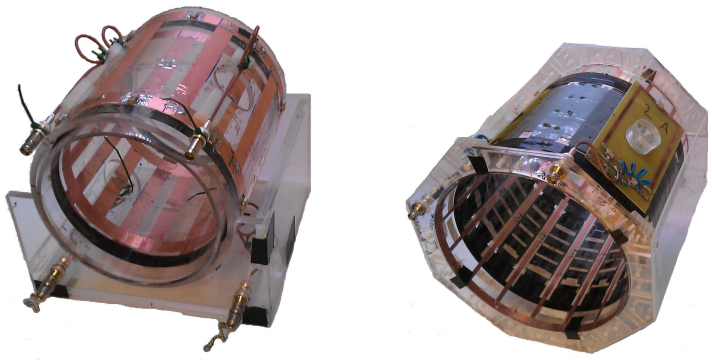

(a) (b)

Figure 2.3: Volume coil examples.

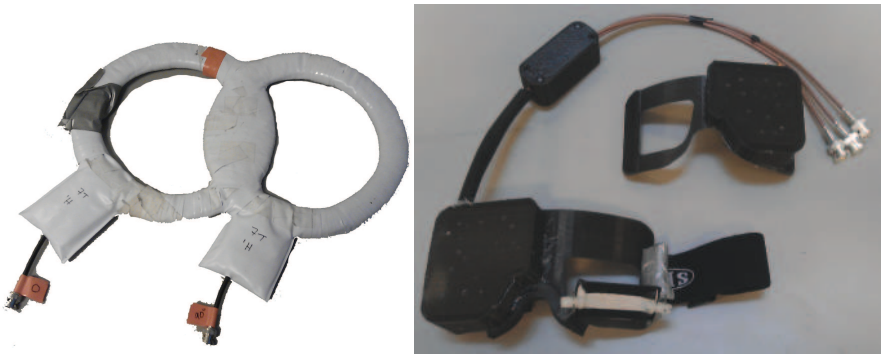

(a) two ringed surface coil (b) left and right eye surface coils

Figure 2.4: Surface coil examples.

High field MRI systems like the 7T scanner at the C. J. Gorter Center do not have an integrated RF-coil (birdcage type) in the bore which most of the 3T scanners do have. Generally, the MR images from a 7T scanner have been obtained using a nonintegrated volume RF-coil, as the homogeneity of the B_1 field generated by a surface coil is usually not sufficient.

Birdcage coils are constructed with multiple parallel conductors symmetrically spaced around the surface of the cylindrical surface, connected by end rings (see Figure 2.5). These are turned into low pass or high pass filter sections by adding capacitors in each conductor, or between each conductor in the end rings, so that at resonance there is a resulting homogeneous B_1 field. When the B_1 field is circularly polarized, the structure can be used as a quadrature coil.

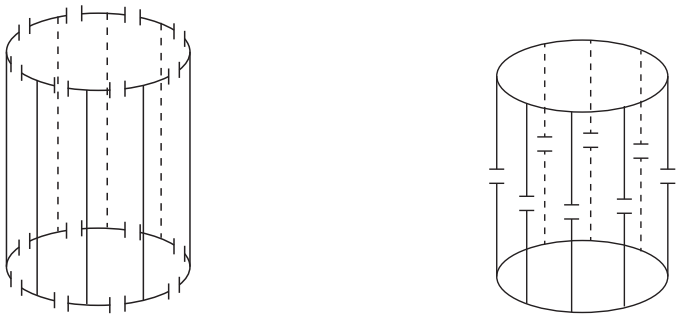

(a) lowpass birdcage coil (b) Highpass birdcage coil

Figure 2.5: Illustration of a low-pass and high-pass volume coils.

2.3 Dielectric resonators

Dielectric resonators are structures that are generally constructed from materials with a high relative permittivity and low loss. This makes them effectively an efficient magnetic storage device. The most common shape for a dielectric resonator (DR) is that of a cylinder. The radiation pattern and the feeding method depend on the mode of interest. Dielectric resonators can support a large number of modes depending on the geometry, dielectric materials, and the excitation source. The modes can be analyzed and indexed in the same way as is done for the dielectric waveguide. The three spatial coordinates are the radius (r), the azimuth (θ), and the axial length (z). This coordinate system is shown in Figure 2.6a.

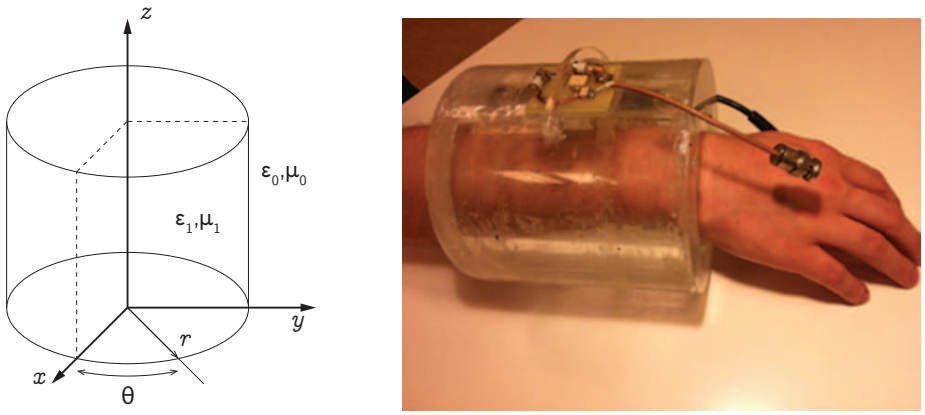

(a) (b)

Figure 2.6: (a) Cylindrical coordinate system. (b) Photograph of a water-based HEM resonator with quadrature inductive feeds.

As mentioned earlier, the most common shape of a dielectric resonator is cylindrical. Figure 2.6b shows a water-based HEM resonator with quadrature inductive feeds. This specific DR was studied by Aussenhofer et al. [6] and computed modal structures of the spatial distribution of the magnetic and electric fields of cylindrical DRs have been presented by Kajfez et al. [7]. Visualization of many modes in a cylindrical DR using MRI has been demonstrated by A.Webb [8].

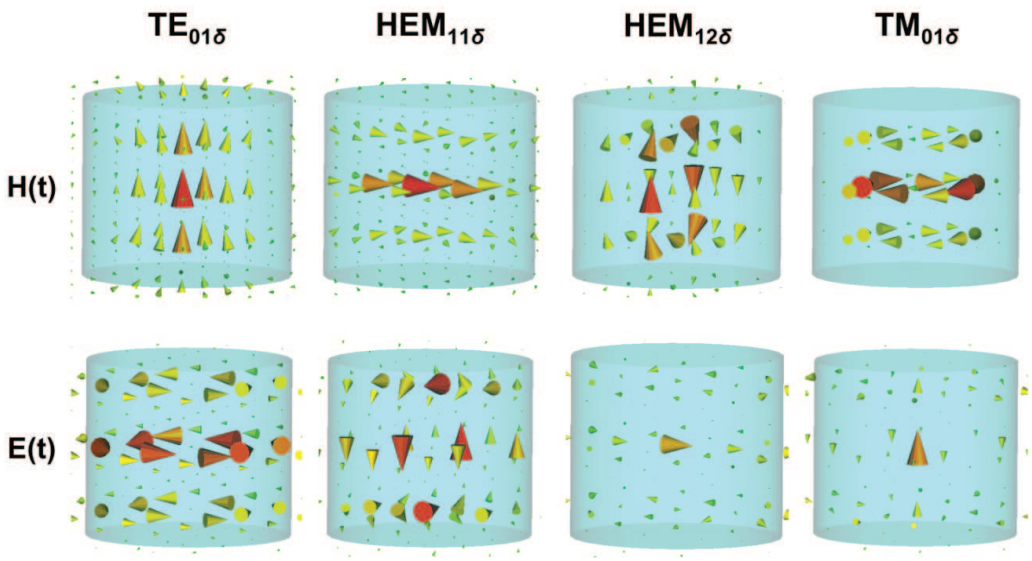

Figure 2.7: Field patterns for the four lowest order modes of a dielectric resonator. Temporally, the magnetic and electric fields are 90 deg out of phase with each other [9].

The resonator modes refer to the specific modes in the dielectric resonator which form stable time invariant field patterns inside the resonator. Cylindrical DRs have transverse electric (TE), transverse magnetic (TM) and hybrid electromagnetic modes (HEM). The different modes are identified by three subscripts, e.g. a TE_{mnp} mode, in which the subscripts m, n, and p denote the number of half wavelength field variations in the azimuthal (θ), radial (r), and height directions, respectively. A subscript (δ) is used when there is less than half a wavelength variation in the transverse fields within the dielectric. The magnetic and electric field patterns of four lower order modes are shown in Figure 2.7. Some of the modes are not optimal for in vivo MR studies due to the perpendicular orientation of their longitudinal axis with respect to the B_0 field of the MR system. One mode, however, can be particularly useful in MR in vivo studies. This mode is called the HEM_{11} mode and can also be operated in quadrature.

High permittivity materials are increasingly more used in high frequency applications like communication devices and MRI systems. This is partially due to their physical robustness and small dimensions compared to that of

more conventional antenna designs created with lumped elements. But the main reason that they are used in these applications is due to their low loss characteristics at those high frequencies. This implies that high permittivity materials can be used for efficiently storing magnetic fields. The losses in these materials at low frequencies or DC will be much greater than that compared to a high frequency application. In this thesis, we therefore focus on designing resonators with high permittivity materials.

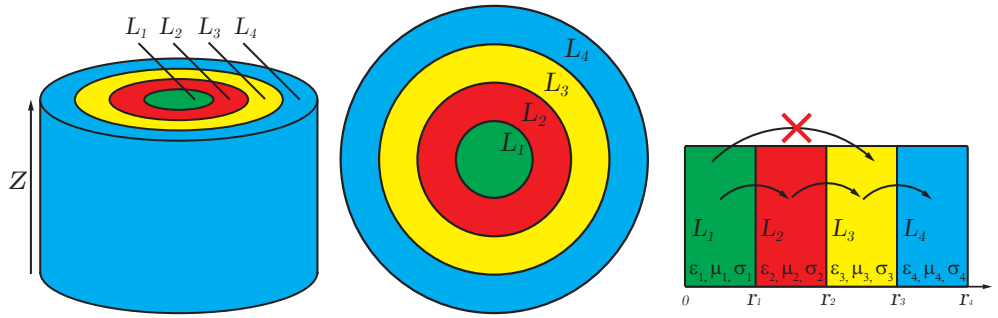

(a) (b) (c)

Figure 2.8: (a) Cylindrical structure with in finite height. (b) Cross section of a cylinder invariant in the z-direction. (c) Use of symmetry and propagating wave cannot "skip" its direct neighbouring layers.

2.4 Cylindrical model

In order to create an analytical model for calculating field distributions in cylindrical structures, we restrict ourselves to two-dimensional resonators that are infinitely long in the z-direction (see Figure 2.8b). as opposed to the real life situation in which the height of the cylinder is finite, of course (Figure 2.8a). This assumption had to be made since this analytical model can only calculate the field distributions correctly if the electromagnetic fields cannot "skip" its direct neighbouring layers while propagating through them. This is illustrated in Figure 2.8c. In other words, the boundary effects in the z-direction are ignored. Furthermore, in our model we consider radially layered media only. All layers are invariant in the z-direction and consist of linear, homogeneous, time-invariant, instantaneously reacting, and isotropic

media. The number of layers is arbitrary, however. Finally, the source used to excite the electromagnetic field is invariant in the z-direction as well and is always located at the interface between two different layers.

Finding the electromagnetic field in the structure described above is clearly a two-dimensional problem now and a detailed solution procedure is described in the upcoming chapters.

Chapter 3

Basic Electromagnetic Field Equations

3.1 Introduction

In this chapter we briefly review the basic electromagnetic field equations. We start with Maxwell's equations in vacuum and take the presence of matter into account by introducing electric and magnetic volume density currents in these equations. The constitutive relations for linear, time invariant, instantaneously reacting, and isotropic media are discussed as well, followed by a discussion on the electromagnetic boundary conditions for source-free interfaces and interfaces that support a surface current.

3.2 Maxwell's equations in differential form

In a vacuum domain, the electromagnetic field is governed by the Maxwell equations

$$-\nabla \times \mathbf{H} + \varepsilon_0 \partial_t \mathbf{E} = \mathbf{0}, \tag{3.2.1}$$

and

$$\nabla \times \mathbf{E} + \mu_0 \partial_t \mathbf{H} = \mathbf{0}. \tag{3.2.2}$$

In these equations, $\mathbf{E}$ is the electric field strength (V/m), $\mathbf{H}$ is the magnetic field strength (A/m), ϵ_0 is the permittivity of vacuum (F/m) and μ_0 is the permeability of vacuum (H/m).

The presence of matter is taken into account by introducing electric and magnetic volume current densities in Maxwell's equations. Denoting the volume density of electric and magnetic current by $\mathbf{J}^{\text{mat}}$ and $\mathbf{K}^{\text{mat}}$, respectively, we postulate that within a material medium the electromagnetic field satisfies the equations

$$-\nabla \times \mathbf{H} + \epsilon_0 \partial_t \mathbf{E} = -\mathbf{J}^{\text{mat}}, \tag{3.2.3}$$

and

$$\nabla \times \mathbf{E} + \mu_0 \partial_t \mathbf{H} = -\mathbf{K}^{\text{mat}}. \tag{3.2.4}$$

These current densities are now written as a superposition of induced and external currents. More precisely, we write

$$\mathbf{J}^{\text{mat}} = \mathbf{J}^{\text{ind}} + \mathbf{J}^{\text{ext}} \tag{3.2.5}$$

and

$$\mathbf{K}^{\text{mat}} = \mathbf{K}^{\text{ind}} + \mathbf{K}^{\text{ext}}, \tag{3.2.6}$$

where the external densities $\mathbf{J}^{\text{ext}}$ and $\mathbf{K}^{\text{ext}}$ are field independent and act as sources for the electromagnetic field, while the induced current densities $\mathbf{J}^{\text{ind}}$ and $\mathbf{K}^{\text{ind}}$ are field dependent and describe the reaction of matter to the presence of an electromagnetic field. It is common practice to rewrite these currents as

$$\mathbf{J}^{\text{ind}} = \mathbf{J} + \partial_t \mathbf{P}, \tag{3.2.7}$$

and

$$\mathbf{K}^{\text{ind}} = \mu_0 \partial_t \mathbf{M}, \tag{3.2.8}$$

where $\mathbf{J}$ is the conduction current (A/m^2), $\mathbf{P}$ is the electric polarization (C/m^2), and $\mathbf{M}$ is the magnetization (A/m). With the introduction of these

new field quantities, Maxwell's equations (3.2.3) and (3.2.4) can be rewritten as

$$-\nabla \times \mathbf{H} + \epsilon_0 \partial_t \mathbf{E} + \mathbf{J} + \partial_t \mathbf{P} = -\mathbf{J}^{\text{ext}}, \tag{3.2.9}$$

and

$$\nabla \times \mathbf{E} + \mu_0 \partial_t \mathbf{H} + \mu_0 \partial_t \mathbf{M} = -\mathbf{K}^{\text{ext}}. \tag{3.2.10}$$

Furthermore, it is customary to introduce the electric and magnetic flux densities as

$$\mathbf{D} = \epsilon_0 \mathbf{E} + \mathbf{P}, \tag{3.2.11}$$

and

$$\mathbf{B} = \mu_0(\mathbf{H} + \mathbf{M}), \tag{3.2.12}$$

respectively, where the electric flux density $\mathbf{D}$ is expressed in $\mathrm{C/m^2}$ and the magnetic flux density $\mathbf{B}$ is expressed in tesla. With the help of these quantities we can rewrite (3.2.9) and (3.2.10) as

$$-\nabla \times \mathbf{H} + \mathbf{J} + \partial_t \mathbf{D} = -\mathbf{J}^{\text{ext}}, \tag{3.2.13}$$

and

$$\nabla \times \mathbf{E} + \partial_t \mathbf{B} = -\mathbf{K}^{\text{ext}}. \tag{3.2.14}$$

The two above equations are known as Maxwell's equations in matter. An overview of all the introduced field quantities is shown in Table 3.1.

Table 3.1: Electromagnetic field quantities and their SI-units

Symbol	Unit	Quantity
$\mathbf{E}$	V/m	electric field strength
$\mathbf{H}$	A/m	magnetic field strength
$\mathbf{D}$	$\mathrm{C/m^2}$	electric flux density
$\mathbf{B}$	T	magnetic flux density
$\mathbf{J}$	$\mathrm{A/m^2}$	electric current density
$\mathbf{K}$	$\mathrm{V/m^2}$	magnetic current density
$\mathbf{P}$	$\mathrm{C/m^2}$	electric polarization
$\mathbf{M}$	A/m	magnetization

Finally, we mention that by applying the divergence operator $(\nabla\cdot)$ to Eqs. (3.2.13) and (3.2.14) we arrive at the so-called compatibility relations

$$\nabla \cdot \mathbf{J} + \partial_t \nabla \cdot \mathbf{D} = -\boldsymbol{\nabla} \cdot \mathbf{J}^{\text{ext}}, \tag{3.2.15}$$

and

$$\partial_t \nabla \cdot \mathbf{B} = -\boldsymbol{\nabla} \cdot \mathbf{K}^{\text{ext}}. \tag{3.2.16}$$

Equation (3.2.15) expresses conservation of charge, while Eq. (3.2.16) shows that the magnetic flux density is divergence free if $\mathbf{K}^{\text{ext}} = \mathbf{0}$.

3.3 The constitutive relations

For most materials, the conduction current $\mathbf{J}$ and the electric flux density $\mathbf{D}$ depend only on the electric field strength, while the magnetic flux density depends only on the magnetic field strength. In this thesis, we restrict ourselves to media of this type. Specifically, we consider linear, time invariant, instantaneously reacting, and isotropic media with constitutive relations

$$\mathbf{J} = \sigma \mathbf{E}, \tag{3.3.1}$$
$$\mathbf{D} = \epsilon \mathbf{E}, \tag{3.3.2}$$

and

$$\mathbf{B} = \mu \mathbf{H}, \tag{3.3.3}$$

where σ, ϵ, and μ, are the conductivity (S/m), permittivity (F/m), and permeability (H/m) of the material. These constitutive parameters are to be considered constant if the medium is homogeneous and in vacuum we obviously have $\sigma = 0$, $\varepsilon = \varepsilon_0$, and $\mu = \mu_0$. Finally, we point out that it is customary to specify permittivity and permeability values in terms of the relative permittivity and permeability defined as

$$\varepsilon_{\text{r}} = \frac{\varepsilon}{\varepsilon_0} \tag{3.3.4}$$

and

$$\mu_{\mathrm{r}} = \frac{\mu}{\mu_0}, \tag{3.3.5}$$

respectively. Note that the relative values of the permeability and permittivity are dimensionless.

Finally, substituting the constitutive relations of Eqs. (3.3.1) – (3.3.3) in Eqs. (3.2.13) and (3.2.14), we arrive at Maxwell's equations in definite form

$$-\nabla \times \mathbf{H} + \sigma \mathbf{E} + \varepsilon \partial_t \mathbf{E} = -\mathbf{J}^{\mathrm{ext}}, \tag{3.3.6}$$

and

$$\nabla \times \mathbf{E} + \mu \partial_t \mathbf{H} = -\mathbf{K}^{\mathrm{ext}}. \tag{3.3.7}$$

3.4 Boundary conditions

Maxwell's equations hold in any domain where the constitutive parameters vary continuously with position. Across interfaces between two different media, however, the parameters exhibit a jump and certain electromagnetic field components show a discontinuous behaviour. Obviously, these electromagnetic field components are then no longer continuously differentiable and Maxwell's equations cease to hold. Relations between the electromagnetic field quantities at either side of the interface are needed and these relations are provided by the electromagnetic boundary conditions.

To introduce these boundary conditions, let $\mathcal{S}$ denote a time invariant interface between two different media. Material 1 occupies a domain $\mathcal{D}^1$ and material 2 occupies a domain $\mathcal{D}^2$. Both domains are located on either side of the interface and $\mathbf{n}$ is the unit normal on $\mathcal{S}$ directed from domain $\mathcal{D}^1$ to domain $\mathcal{D}^2$ (see Figure 3.1). When no external sources are present at the interface $\mathcal{S}$, the tangential components of the electric and magnetic field strength must be continuous across the interface, that is, we must have at the location of the interface

$$\mathbf{n} \times \mathbf{E}^{(2)} - \mathbf{n} \times \mathbf{E}^{(1)} = \mathbf{0}, \tag{3.4.1}$$

and

$$\mathbf{n} \times \mathbf{H}^{(2)} - \mathbf{n} \times \mathbf{H}^{(1)} = \mathbf{0}. \tag{3.4.2}$$

If, however, an electric surface current $\mathbf{J}^{\mathrm{S}}$ is present at the interface, we have

$$\mathbf{n} \times \mathbf{E}^{(2)} - \mathbf{n} \times \mathbf{E}^{(1)} = \mathbf{0}, \tag{3.4.3}$$

and

$$\mathbf{n} \times \mathbf{H}^{(2)} - \mathbf{n} \times \mathbf{H}^{(1)} = \mathbf{J}^{\mathrm{S}}, \tag{3.4.4}$$

while if a magnetic surface current $\mathbf{K}^{\mathrm{S}}$ is present at the interface then

$$\mathbf{n} \times \mathbf{E}^{(2)} - \mathbf{n} \times \mathbf{E}^{(1)} = \mathbf{K}^{\mathrm{S}}, \tag{3.4.5}$$

and

$$\mathbf{n} \times \mathbf{H}^{(2)} - \mathbf{n} \times \mathbf{H}^{(1)} = \mathbf{0}. \tag{3.4.6}$$

These boundary conditions show that an electric surface current produces a jump in the tangential magnetic field strength components, while a magnetic surface current produces a jump in the tangential electric field components.

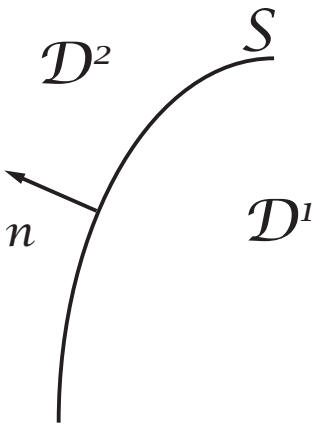

Figure 3.1: Interface between two media with different electromagnetic properties.

3.5 Electromagnetic waves in steady-state

For electromagnetic waves in linear and time invariant media and operating at an angular frequency ω, it is more convenient to work with Maxwell's equations in the frequency-domain. Using an $\exp(-\mathrm{i}\omega t)$ time-dependence, these equations are given by

$$-\nabla \times \hat{\mathbf{H}} + (\sigma - \mathrm{i}\omega\varepsilon)\hat{\mathbf{E}} = -\hat{\mathbf{J}}^{\mathrm{ext}}, \tag{3.5.1}$$

and

$$\nabla \times \hat{\mathbf{E}} - \mathrm{i}\omega\mu\hat{\mathbf{H}} = -\hat{\mathbf{K}}^{\mathrm{ext}}. \tag{3.5.2}$$

From this moment on we drop the hats in our notation, since we will only be working with frequency-domain electromagnetic field quantities.

Chapter 4

Electromagnetic Waves in Cylindrically Layered Media

4.1 Maxwell's equations in cylindrical and polar coordinates

In this thesis, we are interested in cylindrically symmetric configurations. It is therefore convenient to rewrite Maxwell's equations in terms of cylindrical coordinates. For a generic vector $\mathbf{A}$, let A_r, A_θ, and A_z denote its components with respect to the cylindrical basis vectors $\hat{\mathbf{r}}$, $\hat{\boldsymbol{\theta}}$, and $\hat{\mathbf{z}}$, respectively. In the indicated order, these vectors form a right-handed system and the curl operator can be written as

$$\nabla \times \mathbf{A} = \hat{\mathbf{r}} \left(\frac{1}{r} \frac{\partial A_z}{\partial \theta} - \frac{\partial A_\theta}{\partial z} \right) + \hat{\boldsymbol{\theta}} \left(\frac{\partial A_r}{\partial z} - \frac{\partial A_z}{\partial r} \right) + \hat{\mathbf{z}} \frac{1}{r} \left[\frac{\partial}{\partial r}(r A_\theta) - \frac{\partial A_r}{\partial \theta} \right]. \tag{4.1.1}$$

Using this result and assuming that there are no external volume density currents, Maxwell's equations can be written in component form as

$$\frac{1}{r}\frac{\partial H_z}{\partial \theta} - \frac{\partial H_\theta}{\partial z} - (\sigma - \mathrm{i}\omega\varepsilon)E_r = 0, \tag{4.1.2}$$

$$\frac{\partial H_r}{\partial z} - \frac{\partial H_z}{\partial r} - (\sigma - \mathrm{i}\omega\varepsilon)E_\theta = 0, \tag{4.1.3}$$

$$\frac{1}{r}\left[\frac{\partial}{\partial r}(rH_\theta) - \frac{\partial H_r}{\partial \theta}\right] - (\sigma - \mathrm{i}\omega\varepsilon)E_z = 0, \tag{4.1.4}$$

and

$$\frac{1}{r}\frac{\partial E_z}{\partial \theta} - \frac{\partial E_\theta}{\partial z} - \mathrm{i}\omega\mu H_r = 0, \tag{4.1.5}$$

$$\frac{\partial E_r}{\partial z} - \frac{\partial E_z}{\partial r} - \mathrm{i}\omega\mu H_\theta = 0, \tag{4.1.6}$$

$$\frac{1}{r}\left[\frac{\partial}{\partial r}(rE_\theta) - \frac{\partial E_r}{\partial \theta}\right] - \mathrm{i}\omega\mu H_z = 0. \tag{4.1.7}$$

We now make an additional simplification and assume that the media and sources are invariant in the z-direction. The electromagnetic fields are then invariant in the z-direction as well and we may set $\frac{\partial}{\partial z} = 0$ in the above equations. Then Eqs. (4.1.2) – (4.1.7) can be simplified into

$$\frac{1}{r}\frac{\partial H_z}{\partial \theta} - (\sigma - \mathrm{i}\omega\varepsilon)E_r = 0, \tag{4.1.8}$$

$$-\frac{\partial H_z}{\partial r} - (\sigma - \mathrm{i}\omega\varepsilon)E_\theta = 0, \tag{4.1.9}$$

$$\frac{1}{r}\left[\frac{\partial}{\partial r}(rH_\theta) - \frac{\partial H_r}{\partial \theta}\right] - (\sigma - \mathrm{i}\omega\varepsilon)E_z = 0, \tag{4.1.10}$$

and

$$\frac{1}{r}\frac{\partial E_z}{\partial \theta} - \mathrm{i}\omega\mu H_r = 0, \tag{4.1.11}$$

$$-\frac{\partial E_z}{\partial r} - \mathrm{i}\omega\mu H_\theta = 0, \tag{4.1.12}$$

$$\frac{1}{r}\left[\frac{\partial}{\partial r}(rE_\theta) - \frac{\partial E_r}{\partial \theta}\right] - \mathrm{i}\omega\mu H_z = 0. \tag{4.1.13}$$

From the above equations, we observe that E_z, H_r, and H_θ are uncoupled from H_z, E_r, and E_θ. We refer to the first set of field quantities as an *E-polarized field*, since the electric field strength is parallel to the invariance direction. This field is governed by the equations

$$\frac{1}{r}\frac{\partial E_z}{\partial \theta} - \mathrm{i}\omega\mu H_r = 0, \tag{4.1.14}$$

$$-\frac{\partial E_z}{\partial r} - \mathrm{i}\omega\mu H_\theta = 0, \tag{4.1.15}$$

and

$$\frac{1}{r}\left[\frac{\partial}{\partial r}(rH_\theta) - \frac{\partial H_r}{\partial \theta}\right] - (\sigma - \mathrm{i}\omega\varepsilon)E_z = 0. \tag{4.1.16}$$

The second set of field quantities is referred to as an *H-polarized field*, since here the magnetic field is parallel to the invariance direction. This field satisfies the equations

$$\frac{1}{r}\frac{\partial H_z}{\partial \theta} - (\sigma - \mathrm{i}\omega\varepsilon)E_r = 0, \tag{4.1.17}$$

$$-\frac{\partial H_z}{\partial r} - (\sigma - \mathrm{i}\omega\varepsilon)E_\theta = 0, \tag{4.1.18}$$

and

$$\frac{1}{r}\left[\frac{\partial}{\partial r}(rE_\theta) - \frac{\partial E_r}{\partial \theta}\right] - \mathrm{i}\omega\mu H_z = 0. \tag{4.1.19}$$

From this moment on we restrict ourselves to E-polarized fields, since these fields are most relevant for our HEM applicator design tool. We do mention, however, that H-polarized fields can be handled using similar techniques as discussed below for E-polarized waves.

4.2 E-polarized fields in cylindrically layered media

Let us now consider a configuration consisting of N cylindrical layers as shown in Figure 4.1. Each layer occupies the domain

$$\mathcal{D}^{(\ell)} = \{r_{\ell-1} < r < r_\ell,\ 0 \le \theta < 2\pi\} \qquad \text{for } \ell = 1, 2, ..., N$$

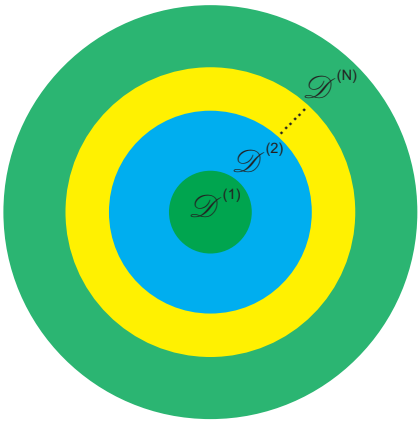

Figure 4.1: N number of cylindrical layers

with $0 = r_0 < r_1 < r_2 < ... < r_{N-1} < r_N$ and $r_N \to \infty$. The constant medium parameters of the ℓth layer are denoted by σ_ℓ and ε_ℓ and the permeability is everywhere equal to the permeability of vacuum. Furthermore, the electromagnetic field in the ℓth layer is written as $\{E_z^{(\ell)}, H_r^{(\ell)}, H_\theta^{(\ell)}\}$. This E-polarized field satisfies the equations

$$\frac{1}{r}\frac{\partial E_z^{(\ell)}}{\partial \theta} - \mathrm{i}\omega\mu_0 H_r^{(\ell)} = 0, \tag{4.2.1}$$

$$-\frac{\partial E_z^{(\ell)}}{\partial r} - \mathrm{i}\omega\mu_0 H_\theta^{(\ell)} = 0, \tag{4.2.2}$$

and

$$\frac{1}{r}\left[\frac{\partial}{\partial r}(rH_\theta^{(\ell)}) - \frac{\partial H_r^{(\ell)}}{\partial \theta}\right] - (\sigma_\ell - \mathrm{i}\omega\varepsilon_\ell)E_z^{(\ell)} = 0, \tag{4.2.3}$$

for $\ell = 1, 2, ..., N$. The electromagnetic field is excited by a z-directed electric surface current $\mathbf{J}^{\mathrm{S}} = J_z^{\mathrm{S}}\hat{\mathbf{z}}$ located at the interface $r = r_i$ between layer i and

layer $i+1$ as shown in Figure 4.2a. Consequently, at this interface we have the boundary conditions

$$\lim_{r\downarrow r_i} E_z^{(i+1)} = \lim_{r\uparrow r_i} E_z^{(i)} \tag{4.2.4}$$

and

$$\lim_{r\downarrow r_i} H_\theta^{(i+1)} - \lim_{r\uparrow r_i} H_\theta^{(i)} = J_z^{\mathrm{S}}. \tag{4.2.5}$$

The tangential electric and magnetic field strengths are continuous at the remaining interfaces, since no other surface currents are present in the configuration (see Figure 4.2b). More precisely, we have

$$\lim_{r\downarrow r_\ell} E_z^{(\ell+1)} = \lim_{r\uparrow r_\ell} E_z^{(\ell)} \tag{4.2.6}$$

and

$$\lim_{r\downarrow r_\ell} H_\theta^{(\ell+1)} = \lim_{r\uparrow r_\ell} H_\theta^{(\ell)} \tag{4.2.7}$$

for all $\ell \neq i$ and $\ell \leq N-1$.

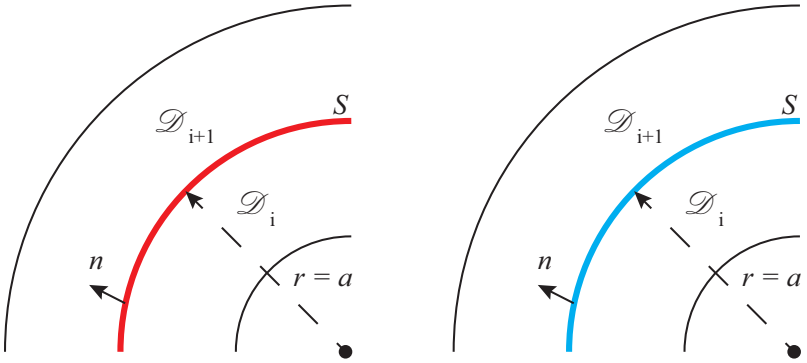

Figure 4.2: (a) Source present at the interface between two layers, (b) Source free interface between two layers

To solve the above set of equations, we first eliminate the magnetic field strength from Eqs. (4.2.1) – (4.2.3). Specifically, substituting

$$H_r^{(\ell)} = \frac{1}{\mathrm{i}\omega\mu_0}\frac{1}{r}\frac{\partial E_z^{(\ell)}}{\partial\theta} \tag{4.2.8}$$

and

$$H_\theta^{(\ell)} = -\frac{1}{\mathrm{i}\omega\mu_0}\frac{\partial E_z^{(\ell)}}{\partial r} \tag{4.2.9}$$

in Eq. (4.2.3) leads to

$$r^2\frac{\partial^2 E_z^{(\ell)}}{\partial r^2} + r\frac{\partial E_z^{(\ell)}}{\partial r} + \frac{\partial^2 E_z^{(\ell)}}{\partial\theta^2} + (k_\ell r)^2 E_z^{(\ell)} = 0, \tag{4.2.10}$$

where we have introduced the wave number of the ℓth layer as

$$k_\ell = [\mathrm{i}\omega\mu_0(\sigma_\ell - \mathrm{i}\omega\varepsilon_\ell)]^{1/2} \qquad \text{with } \mathrm{Im}(k_\ell) \geq 0. \tag{4.2.11}$$

Notice that in a lossless layer ($\sigma_\ell = 0$) this reduces to $k_\ell = \omega/c_\ell$, where $c_\ell = (\varepsilon_\ell\mu_0)^{-1/2}$ is the electromagnetic wave speed in the ℓth layer.

To solve Eq. (4.2.10), we assume that the solution can be written as

$$E_z(r,\theta) = R(r)\Theta(\theta), \tag{4.2.12}$$

where $R(r)$ is a function of r and Θ only depends on θ. Substitution of this trial solution gives

$$r^2\Theta\frac{\mathrm{d}^2 R}{\mathrm{d}r^2} + r\Theta\frac{\mathrm{d}R}{\mathrm{d}r} + R\frac{\mathrm{d}^2\Theta}{\mathrm{d}\theta^2} + (k_\ell r)^2 R\Theta = 0 \tag{4.2.13}$$

and if we divide this result by $R\Theta$, we obtain

$$\frac{r^2}{R}\frac{\mathrm{d}^2 R}{\mathrm{d}r^2} + \frac{r}{R}\frac{\mathrm{d}R}{\mathrm{d}r} + (k_\ell r)^2 + \frac{1}{\Theta}\frac{\mathrm{d}^2\Theta}{\mathrm{d}\theta^2} = 0. \tag{4.2.14}$$

The above equation can only be satisfied if

$$\frac{1}{\Theta}\frac{\mathrm{d}^2\Theta}{\mathrm{d}\theta^2} = -m^2, \tag{4.2.15}$$

and

$$\frac{r^2}{R}\frac{\mathrm{d}^2R}{\mathrm{d}r^2} + \frac{r}{R}\frac{\mathrm{d}R}{\mathrm{d}r} + (k_\ell r)^2 = m^2, \tag{4.2.16}$$

where m^2 is the separation constant. Now Eq. (4.2.15) can be written as

$$\frac{d^2\Theta}{d\theta^2} + m^2\Theta = 0 \tag{4.2.17}$$

and since Θ must be 2π-periodic, we conclude that

$$\Theta(\theta) = \alpha_m e^{\mathrm{i}m\theta}, \tag{4.2.18}$$

where α_m is a constant and m an integer. Furthermore, rewriting Eq. (4.2.16) as

$$r^2\frac{\mathrm{d}^2R}{\mathrm{d}r^2} + r\frac{\mathrm{d}R}{\mathrm{d}r} + [(k_\ell r)^2 - m^2]R = 0 \tag{4.2.19}$$

and writing $R = \hat{R}(k_\ell r)$, we have

$$z^2\frac{\mathrm{d}^2\hat{R}}{\mathrm{d}z^2} + z\frac{\mathrm{d}\hat{R}}{\mathrm{d}z} + (z^2 - m^2)\hat{R} = 0, \tag{4.2.20}$$

with $z = k_\ell r$.

Equation (4.2.20) is Bessel's differential equation. It's general solution can be written in terms of the two linear independent solutions $J_m(z)$ and $Y_m(z)$ known as Bessel functions of the first and second kind, respectively. The subscript m is called the order of the Bessel function.

Alternatively, we can also express the general solution in terms of the so-called Hankel functions $H_m^{(1)}(z)$ and $H_m^{(2)}(z)$. Here, $H_m^{(1)}(z)$ is the Hankel function of the first kind, while $H_m^{(2)}(z)$ is the Hankel function of the second kind [10]. The subscript m again denotes the order of the Hankel function.

The Bessel and Hankel functions are obviously related, since Bessel's differential equation admits only two linearly independent solutions. In particular, we have

$$H_m^{(1)}(z) = J_m(z) + \mathrm{i}Y_m(z) \quad \text{and} \quad H_m^{(2)}(z) = J_m(z) - \mathrm{i}Y_m(z). \tag{4.2.21}$$

In conclusion, we can write the general homogeneous solution of Bessel's equation in terms of Bessel functions as

$$\hat{R}(z) = a_m J_m(z) + b_m Y_m(z), \tag{4.2.22}$$

or in terms of Hankel functions as

$$\hat{R}(z) = c_m H_m^{(1)}(z) + d_m H_m^{(2)}(z), \tag{4.2.23}$$

where a_m, b_m, c_m and d_m are constants. Which functions we use will depend on the layer in which we want to describe the fields.

4.3 General solution

Let us start with layer N, which is the most outer layer. Here, the electromagnetic field can only propagate away from the structure. No waves can propagate towards the layered structure from infinity, since the electric surface current at the ith interface is the only source that is present in the configuration. Given that we use an $\exp(-\mathrm{i}\omega t)$ time convention, we conclude from the asymptotic behavior of the Hankel functions ($z \to \infty$) that waves that are propagating outwardly are described by the Hankel functions of the first kind, while waves that propagate inwardly are described by Hankel functions of the second kind. Since we have only outgoing waves in the outer layer, we therefore expand the electric field strength in this layer as

$$E_z^{(N)}(r,\theta) = \sum_{m=-\infty}^{\infty} C_m H_m^{(1)}(k_N r) e^{\mathrm{i}m\theta} \qquad \text{for } r_{N-1} < r < \infty, \tag{4.3.1}$$

where the C_m are the expansion coefficients. Furthermore, the magnetic field strength $H_\theta^{(N)}$, which is tangential to the interface at $r = r_{N-1}$, is also required in the boundary conditions for the electromagnetic field quantities. Substituting the electric field expansion in Eq. (4.2.9), this field component is obtained as

$$H_\theta^{(N)}(r,\theta) = \frac{\mathrm{i}k_N}{\omega\mu_0} \sum_{m=-\infty}^{\infty} C_m H_m^{(1)\prime}(k_N r) e^{\mathrm{i}m\theta} \qquad \text{for } r_{N-1} < r < \infty, \tag{4.3.2}$$

where the prime indicates the derivative of the Hankel function with respect to its argument. Now in the remaining layers, the electromagnetic field consists of reflected and transmitted waves that propagate outward and inwardly. In these layers, we therefore expand the electric field in terms of Bessel functions of the first and second kind. Specifically, the electric field in the ℓth layer ($1 \le \ell < N$) is written as

$$E_z^{(\ell)}(r,\theta) = \sum_{m=-\infty}^{\infty} [A_m^{(\ell)} J_m(k_\ell r) + B_m^{(\ell)} Y_m(k_\ell r)] e^{\mathrm{i}m\theta} \quad \text{for } r_{\ell-1} < r < r_\ell, \tag{4.3.3}$$

where $A_m^{(\ell)}$ and $B_m^{(\ell)}$ are the expansion coefficients of the electric field within the ℓth layer. The corresponding magnetic field component tangential to the interfaces is found from Eq. (4.2.9) as

$$H_\theta^{(\ell)} = \frac{\mathrm{i}k_\ell}{\omega\mu_0} \sum_{m=-\infty}^{\infty} [A_m^{(\ell)} J_m'(k_\ell r) + B_m^{(\ell)} Y_m'(k_\ell r)] e^{\mathrm{i}m\theta} \quad \text{for } r_{\ell-1} < r < r_\ell. \tag{4.3.4}$$

These are the general expansions for the field components that are tangential to the interfaces. For the first layer, however, these expansions simplify somewhat, since we know that the Bessel function of the second kind is

singular at the origin. From this it follows that we must set $B_m^{(1)} = 0$ for all m and our tangential field expansions in this layer become

$$E_z^{(1)}(r,\theta) = \sum_{m=-\infty}^{\infty} A_m^{(1)} J_m(k_\ell r) e^{\mathrm{i}m\theta} \quad \text{for } 0 \le r < r_1, \tag{4.3.5}$$

and

$$H_\theta^{(1)}(r,\theta) = \frac{\mathrm{i}k_\ell}{\omega\mu_0} \sum_{m=-\infty}^{\infty} A_m^{(1)} J_m'(k_\ell r) e^{\mathrm{i}m\theta} \quad \text{for } 0 \le r < r_1. \tag{4.3.6}$$

We now have a complete field description in each layer of our configuration. To arrive at a system of equations for the expansion coefficients, we invoke the boundary conditions which hold upon crossing an interface between two different layers.

4.3.1 Source-free boundary conditions

In Section 4.2 we mentioned that the z-component of the electric field strength and the θ-component of the magnetic field strength should be continuous across a source-free interface. In particular, at the source-free interface $r = r_\ell$ between layers ℓ and $\ell + 1$, we have

$$\lim_{r \downarrow r_\ell} E_z^{(\ell+1)} = \lim_{r \uparrow r_\ell} E_z^{(\ell)} \tag{4.3.7}$$

and

$$\lim_{r \downarrow r_\ell} H_\theta^{(\ell+1)} = \lim_{r \uparrow r_\ell} H_\theta^{(\ell)} \tag{4.3.8}$$

Substitution of the field expansions in the boundary condition for the electric field gives

$$\begin{aligned} &\sum_{m=-\infty}^{\infty} \left[A_m^{(\ell+1)} J_m(k_{\ell+1} r_\ell) + B_m^{(\ell+1)} Y_m(k_{\ell+1} r_\ell) \right] e^{\mathrm{i}m\theta} = \\ &\sum_{m=-\infty}^{\infty} \left[A_m^{(\ell)} J_m(k_\ell r_\ell) + B_m^{(\ell)} Y_m(k_\ell r_\ell) \right] e^{\mathrm{i}m\theta} \end{aligned} \tag{4.3.9}$$

Multiplying this equation by $e^{-\mathrm{i}n\theta}$, integrating the result from $\theta = 0$ to $\theta = 2\pi$, and using the result

$$\int_{\theta=0}^{2\pi} e^{\mathrm{i}(m-n)\theta}\,\mathrm{d}\theta = \begin{cases} 2\pi & \text{if } n = m, \\ 0 & \text{if } n \neq m, \end{cases} \tag{4.3.10}$$

we arrive at

$$A_m^{(\ell+1)} J_m(k_{\ell+1} r_\ell) + B_m^{(\ell+1)} Y_m(k_{\ell+1} r_\ell) = A_m^{(\ell)} J_m(k_\ell r_\ell) + B_m^{(\ell)} Y_m(k_\ell r_\ell), \tag{4.3.11}$$

which has to hold for each m and at any source-free interface $r = r_\ell$.

Following a similar procedure for the magnetic field strength boundary condition, we obtain

$$\frac{\mathrm{i}k_{\ell+1}}{\omega\mu_0}\left[A_m^{(\ell+1)} J'_m(k_{\ell+1} r_\ell) + B_m^{(\ell+1)} Y'_m(k_{\ell+1} r_\ell)\right] = \frac{\mathrm{i}k_\ell}{\omega\mu_0}\left[A_m^{(\ell)} J'_m(k_\ell r_\ell) + B_m^{(\ell)} Y'_m(k_\ell r_\ell)\right]. \tag{4.3.12}$$

This is the second equation that has to hold at a source-free interface $r = r_\ell$. Finally, as mentioned above, for $\ell = 1$ we have $B_m^{(\ell)} = B_m^{(1)} = 0$ for all m, since Y_m is singular at the origin.

4.3.2 Boundary conditions with an external electric-current sheet present

As we have seen, if an external electric-current surface source is present at the interface $r = r_i$, the boundary conditions for the tangential electric and magnetic field strength are given by

$$\lim_{r\downarrow r_i} E_z^{(i+1)} = \lim_{r\uparrow r_i} E_z^{(i)} \tag{4.3.13}$$

and

$$\lim_{r\downarrow r_i} H_\theta^{(i+1)} - \lim_{r\uparrow r_i} H_\theta^{(i)} = J_z^{\mathrm{S}}. \tag{4.3.14}$$

Here, $J_z^{\mathrm{S}} = J_z^{\mathrm{S}}(\theta)$ is the surface current present at $r = r_i$ which depends on θ only.

Since the boundary condition for the electric field is the same as in the source-free case, we can simply repeat the steps from the previous subsection to obtain the boundary condition

$$A_m^{(i+1)} J_m(k_{i+1} r_i) + B_m^{(i+1)} Y_m(k_{i+1} r_i) = A_m^{(i)} J_m(k_i r_i) + B_m^{(i)} Y_m(k_i r_i). \quad (4.3.15)$$

Again, this equation should hold for each $m \in \mathbb{Z}$.

For the magnetic field boundary condition, we proceed as follows. First, we substitute the field expansions in Eq. (4.3.14). This gives

$$\begin{aligned} &\frac{\mathrm{i}k_{i+1}}{\omega\mu_0} \sum_{m=-\infty}^{\infty} \left[A_m^{(i+1)} J'_m(k_{i+1} r_i) + B_m^{(i+1)} Y'_m(k_{i+1} r_i)\right] e^{\mathrm{i}m\theta} - \\ &\frac{\mathrm{i}k_i}{\omega\mu_0} \sum_{m=-\infty}^{\infty} \left[A_m^{(i)} J'_m(k_i r_i) + B_m^{(i)} Y'_m(k_i r_i)\right] e^{\mathrm{i}m\theta} = J_z^{\mathrm{S}}(\theta). \end{aligned} \quad (4.3.16)$$

Multiplying this equation by $e^{-\mathrm{i}n\theta}$, integrating from $\theta = 0$ to $\theta = 2\pi$, and using Eq. (4.3.10), we arrive at

$$\begin{aligned} &\frac{\mathrm{i}k_{i+1}}{\omega\mu_0}[A_m^{(i+1)} J'_m(k_{i+1} r_i) + B_m^{(i+1)} Y'_m(k_{i+1} r_i)] \\ &\qquad - \frac{\mathrm{i}k_i}{\omega\mu_0} \left[A_m^{(i)} J'_m(k_i r_i) + B_m^{(i)} Y'_m(k_i r_i)\right] = j_m^{\mathrm{S}}, \end{aligned} \quad (4.3.17)$$

where we have introduced

$$j_m^{\mathrm{S}} = \frac{1}{2\pi} \int_{\theta=0}^{2\pi} J_z^{\mathrm{S}}(\theta) e^{-\mathrm{i}m\theta} \, \mathrm{d}\theta. \quad (4.3.18)$$

Equation (4.3.17) should hold for each m at the interface $r = r_i$. Note that the external source J_z^{S} determines which expansion coefficients are nonzero.

4.4 Example: scattering formalism for a five layer configuration

Let us now put the general equations of the previous section into action. To this end, we consider the configuration shown in Figure 4.3 consisting of five

layers. Each layer has its own constant medium parameters and the external electric-current source is located at the interface $r = r_3$ between layer 3 and 4.

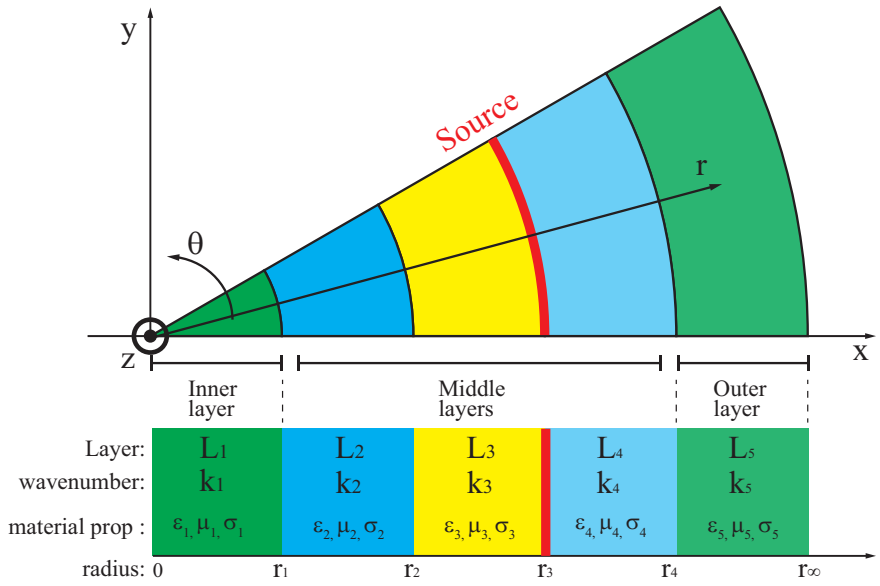

Figure 4.3: Cylindrical configuration consisting of five layers.

Since the interface $r = r_1$ is source-free, we have

$$A_m^{(2)} J_m(k_2 r_1) + B_m^{(2)} Y_m(k_2 r_1) - A_m^{(1)} J_m(k_1 r_1) = 0 \qquad (4.4.1)$$

and

$$\frac{\mathrm{i}k_2}{\omega\mu_0} A_m^{(2)} J'_m(k_2 r_1) + \frac{\mathrm{i}k_2}{\omega\mu_0} B_m^{(2)} Y'_m(k_2 r_1) - \frac{\mathrm{i}k_1}{\omega\mu_0} A_m^{(1)} J'_m(k_1 r_1) = 0, \qquad (4.4.2)$$

where we have taken into account that $B_m^{(1)} = 0$ for each $m \in \mathbb{Z}$.

The interface $r = r_2$ is source-free as well and therefore

$$A_m^{(3)} J_m(k_3 r_2) + B_m^{(3)} Y_m(k_3 r_2) - A_m^{(2)} J_m(k_2 r_2) - B_m^{(2)} Y_m(k_2 r_2) = 0 \qquad (4.4.3)$$

and

$$\begin{aligned}\frac{\mathrm{i}k_3}{\omega\mu_0}A_m^{(3)}J'_m(k_3r_2)+\frac{\mathrm{i}k_3}{\omega\mu_0}B_m^{(3)}Y'_m(k_3r_2)\\ -\frac{\mathrm{i}k_2}{\omega\mu_0}A_m^{(2)}J'_m(k_2r_2)-\frac{\mathrm{i}k_2}{\omega\mu_0}B_m^{(2)}Y'_m(k_2r_2)=0.\end{aligned} \tag{4.4.4}$$

The external electric surface current is located at $r = r_3$. This leads to the boundary conditions

$$A_m^{(4)}J_m(k_4r_3)+B_m^{(4)}Y_m(k_4r_3)-A_m^{(3)}J_m(k_3r_3)-B_m^{(3)}Y_m(k_3r_3)=0 \tag{4.4.5}$$

and

$$\begin{aligned}\frac{\mathrm{i}k_4}{\omega\mu_0}A_m^{(4)}J'_m(k_4r_3)+\frac{\mathrm{i}k_4}{\omega\mu_0}B_m^{(4)}Y'_m(k_4r_3)\\ -\frac{\mathrm{i}k_3}{\omega\mu_0}A_m^{(3)}J'_m(k_3r_3)-\frac{\mathrm{i}k_3}{\omega\mu_0}B_m^{(3)}Y'_m(k_3r_3)=j_m^{\mathrm{S}}.\end{aligned} \tag{4.4.6}$$

Finally, the interface $r = r_4$ is source-free again and therefore we have

$$C_mH_m^{(1)}(k_5r_4)-A_m^{(4)}J_m(k_4r_4)-B_m^{(4)}Y_m(k_4r_4)=0 \tag{4.4.7}$$

and

$$\frac{\mathrm{i}k_5}{\omega\mu_0}C_mH_m^{(1)\prime}(k_5r_4)-\frac{\mathrm{i}k_4}{\omega\mu_0}A_m^{(4)}J'_m(k_4r_4)-\frac{\mathrm{i}k_4}{\omega\mu_0}B_m^{(4)}Y'_m(k_4r_4)=0. \tag{4.4.8}$$

Arranging now all the unknown expansion coefficients in the 8-by-1 column vector

$$\mathsf{x}_m=[A_m^{(1)},A_m^{(2)},B_m^{(2)},A_m^{(3)},B_m^{(3)},A_m^{(4)},B_m^{(4)},C_m]^T \tag{4.4.9}$$

and introducing the source vector

$$\mathsf{b}_m=-\mathrm{i}\omega\mu_0 j_m^{\mathrm{S}}\mathsf{e}_6, \tag{4.4.10}$$

where e_6 is the 6th column of the 8-by-8 identity matrix, we can write all equations more compactly as

$$\mathsf{A}_m\mathsf{x}_m=\mathsf{b}_m, \tag{4.4.11}$$

where we have introduced the 8-by-8 system matrix A_m whose columns are given by

$$\mathsf{A}_m(:,1) = \begin{pmatrix} -J_m(k_1 r_1) \\ -k_1 J_m'(k_1 r_1) \\ 0 \\ 0 \\ 0 \\ 0 \\ 0 \\ 0 \end{pmatrix}, \quad \mathsf{A}_m(:,2) = \begin{pmatrix} J_m(k_2 r_1) \\ k_2 J_m'(k_2 r_1) \\ -J_m(k_2 r_2) \\ -k_2 J_m'(k_2 r_2) \\ 0 \\ 0 \\ 0 \\ 0 \end{pmatrix}, \tag{4.4.12}$$

$$\mathsf{A}_m(:,3) = \begin{pmatrix} Y_m(k_2 r_1) \\ k_2 Y_m'(k_2 r_1) \\ -Y_m(k_2 r_2) \\ -k_2 Y_m'(k_2 r_2) \\ 0 \\ 0 \\ 0 \\ 0 \end{pmatrix}, \quad \mathsf{A}_m(:,4) = \begin{pmatrix} 0 \\ 0 \\ J_m(k_3 r_2) \\ k_3 J_m'(k_3 r_2) \\ -J_m(k_3 r_3) \\ -k_3 J_m'(k_3 r_3) \\ 0 \\ 0 \end{pmatrix}, \tag{4.4.13}$$

$$\mathsf{A}_m(:,5) = \begin{pmatrix} 0 \\ 0 \\ Y_m(k_3 r_2) \\ k_3 Y_m'(k_3 r_2) \\ -Y_m(k_3 r_3) \\ -k_3 Y_m'(k_3 r_3) \\ 0 \\ 0 \end{pmatrix}, \quad \mathsf{A}_m(:,6) = \begin{pmatrix} 0 \\ 0 \\ 0 \\ 0 \\ J_m(k_4 r_3) \\ k_4 J_m'(k_4 r_3) \\ -J_m(k_4 r_4) \\ -k_4 J_m'(k_4 r_4) \end{pmatrix}, \tag{4.4.14}$$

$$\mathsf{A}_m(:,7) = \begin{pmatrix} 0 \\ 0 \\ 0 \\ 0 \\ Y_m(k_4 r_3) \\ k_4 Y_m'(k_4 r_3) \\ -Y_m(k_4 r_4) \\ -k_4 Y_m'(k_4 r_4) \end{pmatrix}, \quad \mathsf{A}_m(:,8) = \begin{pmatrix} 0 \\ 0 \\ 0 \\ 0 \\ 0 \\ 0 \\ H_m^{(1)}(k_5 r_4) \\ k_5 H_m^{(1)\prime}(k_5 r_4) \end{pmatrix}. \tag{4.4.15}$$

Clearly, matrix A_m is of the form

$$\mathsf{A}_m = \begin{bmatrix} \mathsf{x} & \mathsf{x} & \mathsf{x} & 0 & 0 & 0 & 0 & 0 \\ \mathsf{x} & \mathsf{x} & \mathsf{x} & 0 & 0 & 0 & 0 & 0 \\ 0 & \mathsf{x} & \mathsf{x} & \mathsf{x} & \mathsf{x} & 0 & 0 & 0 \\ 0 & \mathsf{x} & \mathsf{x} & \mathsf{x} & \mathsf{x} & 0 & 0 & 0 \\ 0 & 0 & 0 & \mathsf{x} & \mathsf{x} & \mathsf{x} & \mathsf{x} & 0 \\ 0 & 0 & 0 & \mathsf{x} & \mathsf{x} & \mathsf{x} & \mathsf{x} & 0 \\ 0 & 0 & 0 & 0 & 0 & \mathsf{x} & \mathsf{x} & \mathsf{x} \\ 0 & 0 & 0 & 0 & 0 & \mathsf{x} & \mathsf{x} & \mathsf{x} \end{bmatrix}, \tag{4.4.16}$$

where a cross denotes a nonzero entry. This structure shows how the blocks corresponding to different layers are coupled.

Assuming that A_m is nonsingular, we observe that if $\mathsf{b}_m = \mathsf{0}$ for a particular value of m then $\mathsf{x}_m = \mathsf{0}$ as well and all the corresponding expansion coefficients vanish. For example, if the external electric surface current is of the form

$$J_z^{\mathrm{S}}(\theta) = J^{\mathrm{amp}} \cos(\theta) \tag{4.4.17}$$

with $J^{\mathrm{amp}} > 0$, then

$$j_m^{\mathrm{S}} = \frac{1}{2} J^{\mathrm{amp}} (\delta_{m,-1} + \delta_{m,1}), \tag{4.4.18}$$

where the delta functions are Kronecker delta's. In this case, only the source vectors b_{-1} and b_1 are nonzero and therefore all expansion coefficients with indices $m \neq \pm 1$ vanish.

In conclusion, after specifying the external electric-current surface source $J_z^{\mathrm{S}}(\theta)$, we can determine which modes will be excited by computing j_m^{S}. The corresponding source vector b_m is then known as well and the corresponding expansion coefficients can be determined by solving Eq. (4.4.11).

Chapter 5

Validation of The Analytical Matlab Simulation Tool

In this chapter we present the results of a Matlab program which is based on the analytical model discussed in the previous chapters. The program determines the EM field distributions by evaluating the structure of the resonator, the excitation source and material properties of each individual cylindrical layer. The parameters which the user can adjust are the number of layers in the dielectric resonator, the radii of the different layers, the location and amplitude of the excitation source, and the electromagnetic properties of the materials in each layer (relative permittivity $\varepsilon_{\mathrm{r};\ell}$ and conductivity σ_ℓ). In all examples, the external electric surface current is of the form

$$J_z^{\mathrm{S}} = J^{\mathrm{amp}} \cos(\theta)$$

with $J^{\mathrm{amp}} = 1$ A/m and operating at a frequency of 298 MHz. The program determines the electromagnetic field components which are tangential to the interfaces using the scattering formalism discussed in the previous chapter.

Three sets of simulations will be done in order to verify and validate that the analytical simulation tool functions properly and that the outcomes are comparable to that of a commonly used numerical solver. We also will validate that the z-invariant model can be used for determining the electromagnetic fields in cylindrical structures with a finite height and that we can use this

tool to help us design a practical HEM resonator which can be used in MRI experiments.

In the first set of simulations we will verify that there are no discontinuities at the interfaces between two adjacent layers. The only exception will be the expected discontinuity of the magnetic field (H_θ) at the interface where the current source is placed. We will run these simulations on multiple homogeneous and inhomogeneous cylindrical structures, where we will change some parameters such as the relative permittivity and layer thickness. We also will demonstrate that we can add losses to the dielectric materials; this is something that the numerical eigenmode solver from CST cannot do. After we have shown that the analytical tool functions properly we will compare the results to an identical cylindrical setup that is simulated with the numerical eigenmode solver from CST.

In the second set of simulations we will verify that the model can be used in z-variant structures of a certain height. We will do this by simulating multiple cylindrical structures with different heights. These simulations will be done in the CST eigenmode solver. These simulations will show that only the amplitude of the electromagnetic fields will change and not the shape and trend of the electromagnetic field distributions.

In the third and last set of simulations we will show that the analytical simulation tool can aid us in the design of a practical HEM dielectric resonator that can be used in MRI experiments.

5.1 Set 1: Validation of the analytical simulation tool

As mentioned in Section 2.4, we only have to simulate the electromagnetic field distribution from the center to the outer radius of the cylindrical configuration due to the circular symmetrical features of the cylindrical configuration. Figure 5.1 illustrates the field distributions from a simulation of an arbitrary dielectric resonator – only the calculated magnetic fields are shown.

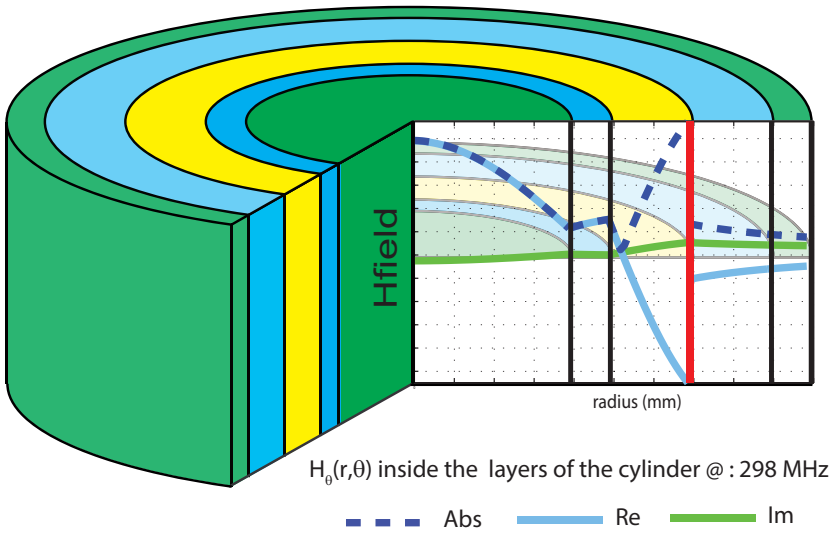

Figure 5.1: Simulation of an arbitrary dielectric resonator with a source (J_z^{S}) between the third and fourth layer. Only the magnitude of the calculated magnetic fields are shown.

In order to show that there are no discontinuities at the boundaries, we first simulate a homogeneous lossless cylindrical structure with 5 layers. All layers have a relative permittivity of 50 or 200. These values are chosen because the relative permittivity of human tissue is approximately 50 and the high permittivity bags ($BaTiO_3$) used in the Gorter center for improving MR image quality have an relative permittivity of about 200. These bags consist of a mixture of regular tap water and $BaTiO_3$ and can have a varying thickness. The relative permittivity of the bags ranges typically from 100 to 300 [11]. The values chosen for the conductivity (σ) are 0.1 S/m and 0.77 S/m. We deliberately take a small value for the conductivity (σ = 0.1 S/m) to verify that highly resonant structures do not prolong the needed simulation time, which is the case in the numerical solvers. The other chosen conductivity is the same as that in muscle tissue ($\sigma_{\mathrm{muscle}} = 0.77$ S/m).

After the simulation of the homogeneous cylinder we simulate an inhomogeneous cylinder. This will verify that there are also no discontinuities when an inhomogeneous cylinder is simulated. This simulation is done both with lossless and lossy dielectrics.

In MRI scans there is usually a varying air-gap between the coil and the tissue. Therefore, a simulation is carried out in which we vary the air-gap between tissue (inner layer) and the high permittivity dielectric bags. This simulation will give more insight on how the size of an air-gap may influence the field distributions in each of the layers of the cylindrical structure.

In the last simulation the thickness of the dielectric bags is varied. This example will illustrate how varying the thickness of the dielectric bags will influence the fields inside the layers of the cylindrical structure.

5.1.1 Homogeneous cylindrical structure

Figure 5.2 shows the field distributions in a cylindrical structure where the material in each layer possesses the same electromagnetic properties. This creates a homogeneous structure which can be considered as a cylinder consisting of only one layer with a source embedded somewhere in this cylindrical structure. The materials in this figure are lossless ($\sigma = 0$). The only difference between the simulated cylindrical structure in Figure 5.2a and 5.2b is the relative permittivity of the layers. The layers shown in Figure 5.2a have a relative permittivity of 50, while all of the layers in Figure 5.2b have a relative permittivity of 200. We observe that there are no jumps across different layers with the same medium parameters and the jump in the tangential component of the magnetic field is correctly modelled as well. The magnitude of this jump is exactly the same as the amplitude of the source (J^{amp}) which in this case is 1 A/m.

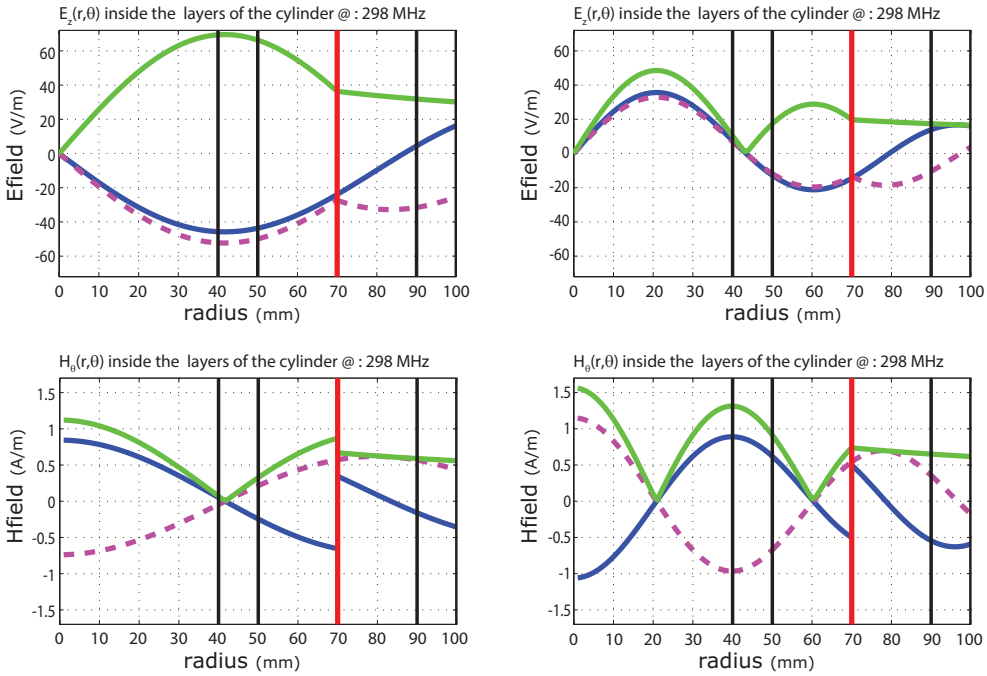

	L_1	L_2	L_3	L_4	L_5
rad (mm)	40	50	70	90	100
ε_r	50	50	50	50	50
μ_r	1	1	1	1	1
σ	0	0	0	0	0

(a)

	L_1	L_2	L_3	L_4	L_5
rad (mm)	40	50	70	90	100
ε_r	200	200	200	200	200
μ_r	1	1	1	1	1
σ	0	0	0	0	0

(b)

Figure 5.2: (a) Homogeneous lossless dielectric layers with $\varepsilon_r = 50$, (b) homogeneous lossless dielectric layers with $\varepsilon_r = 200$.

The z-component of the electric field strength and the θ-component of the magnetic field strength are presented in separate graphs and a table in which we specify the dimensions of the layers. The electromagnetic properties of the materials are presented underneath these graphs. Finally, a vertical black line indicates the boundary of a layer while a vertical red line represents the location of the excitation source (J_z^S). From the above figure it is clear that the wavelength of an electromagnetic wave depends on the value of the relative permittivity of the material where the wave is passing through. The wave-

length inside a certain material can be calculated with the equation

$$\lambda = \frac{2\pi}{\omega\sqrt{\mu_0\mu_\mathrm{r}\epsilon_0\epsilon_\mathrm{r}}}. \tag{5.1.1}$$

Figure 5.3 illustrates field distributions of the same homogeneous cylindrical structure as in Figure 5.2 with the exception that all layers now have some losses, meaning $\sigma \neq 0$. The layers used in Figure 5.3a has a conductivity $\sigma = 0.1$ S/m, while all the layers shown in Figure 5.3b have a conductivty $\sigma = 0.77$ S/m. Again, we do not observe any field discontinuities in the tangential components. Furthermore, if we compare the field distributions in Figures 5.2a, 5.3a, and 5.3b we can conclude that the magnitude of the electric (E_z) and the magnetic H_θ field will decrease when we introduce lossy materials inside the cylindrical layers. This is what we would expect when losses are introduced to dielectric materials. The energy loss will be converted into heat.

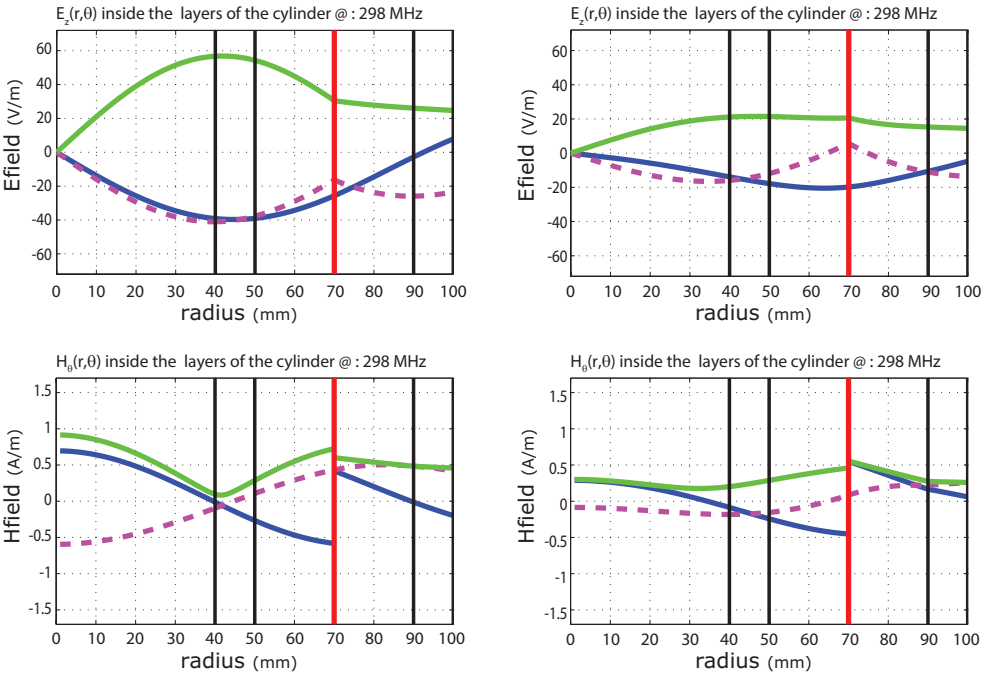

	L_1	L_2	L_3	L_4	L_5
rad (mm)	40	50	70	90	100
ε_r	50	50	50	50	50
μ_r	1	1	1	1	1
σ	0.1	0.1	0.1	0.1	0.1

(a)

	L_1	L_2	L_3	L_4	L_5
rad (mm)	40	50	70	90	100
ε_r	50	50	50	50	50
μ_r	1	1	1	1	1
σ	0.77	0.77	0.77	0.77	0.77

(b)

Figure 5.3: (a) Homogeneous lossy dielectric layers with a relative permittivity $\varepsilon_r = 50$ and a conductivity $\sigma = 0.1$ S/m, (b) homogeneous lossy dielectric layers with a relative permittivity $\varepsilon_r = 50$ and a conductivity $\sigma = 0.77$ S/m.

5.1.2 Inhomogeneous cylindrical structure

The graphs in Figures 5.4 and 5.5 show the field distributions in a cylindrical structure with inhomogeneous dielectric layers. While the dielectric layers in Figure 5.4 comprise of lossless materials, the dielectric layers in Figure 5.5 do possess some lossy materials. If we compare the field distribution of

two cylindrical structures where one consists of homogeneous dielectric layers (Figure. 5.2) and the other consists of inhomogeneous dielectric layers (Figure 5.4) we can determine that the two field distributions are significantly different. In these examples the materials possess no electromagnetic losses. If we look more closely to an example with lossy inhomogeneous dielectrics as was shown in Figures 5.5a and 5.5b, we can establish that the relative permittivity of the materials has the largest influence on the field distributions. It should be noted that electromagnetic losses certainly do have some influence on the magnitude of the electromagnetic field strength but in this particular example the distributions are mainly influenced by the permittivity.

Furthermore, when the relative permittivity is increased in a layer the magnetic field will be more present in the layers that have a higher relative permittivity. This can be seen if we compare the magnitude of the H-field in the third layer (50 mm - 70 mm) of Figure 5.4a and 5.4b.

The Figures 5.4 and 5.5 also show that for inhomogeneous cylindrical structures the relative permittivity in the layers has more influence on the shape and trend of the field distribution than the losses (σ) in the dielectric material. The losses will only influence the magnitude of the electromagnetic field distribution.

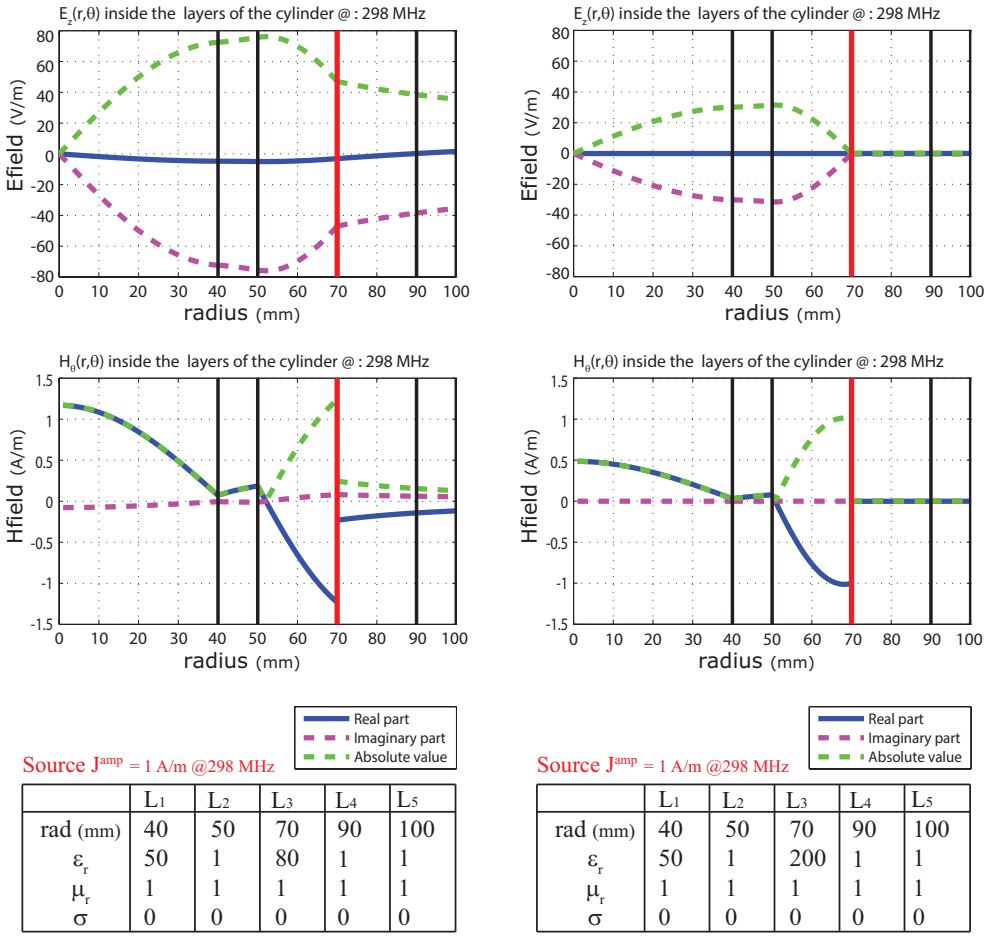

	L_1	L_2	L_3	L_4	L_5
rad (mm)	40	50	70	90	100
ε_r	50	1	80	1	1
μ_r	1	1	1	1	1
σ	0	0	0	0	0

(a)

	L_1	L_2	L_3	L_4	L_5
rad (mm)	40	50	70	90	100
ε_r	50	1	200	1	1
μ_r	1	1	1	1	1
σ	0	0	0	0	0

(b)

Figure 5.4: Field distributions in two different inhomogeneous, lossless, and layered cylindrical structures.

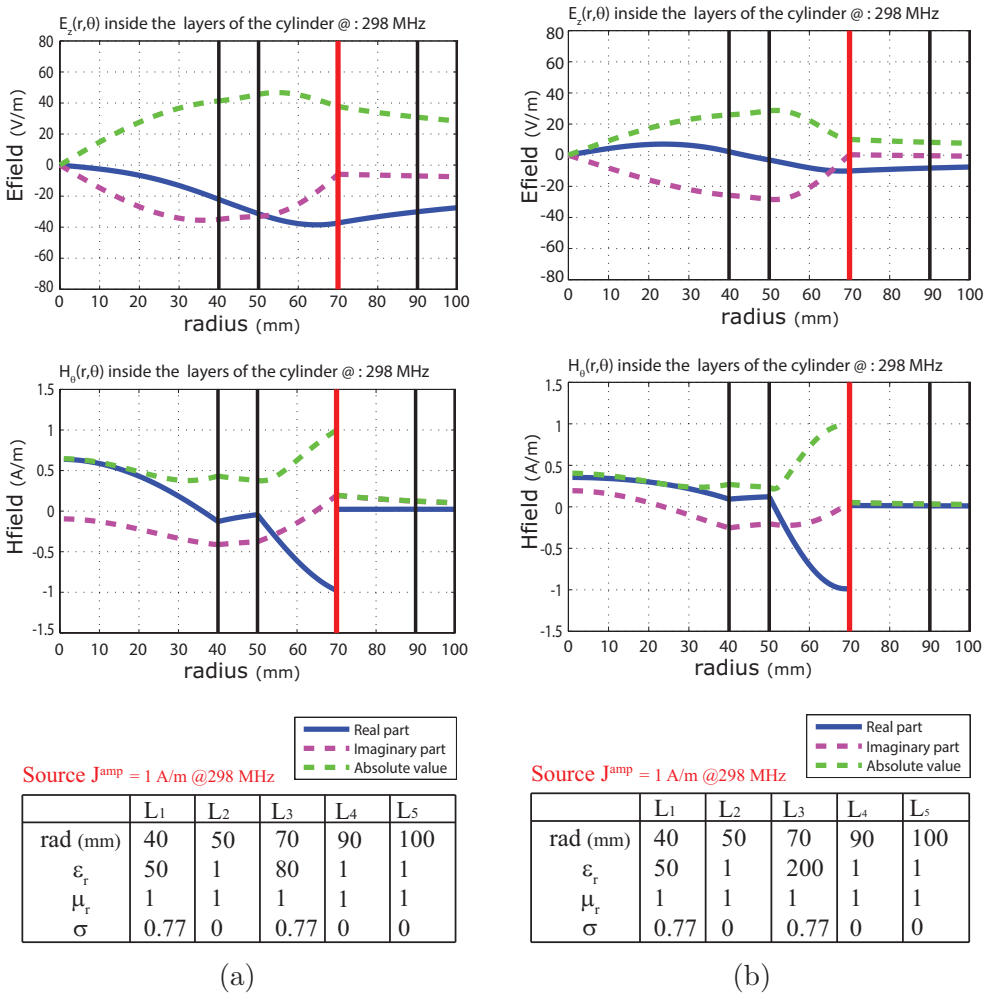

	L_1	L_2	L_3	L_4	L_5
rad (mm)	40	50	70	90	100
ε_r	50	1	80	1	1
μ_r	1	1	1	1	1
σ	0.77	0	0.77	0	0

(a)

	L_1	L_2	L_3	L_4	L_5
rad (mm)	40	50	70	90	100
ε_r	50	1	200	1	1
μ_r	1	1	1	1	1
σ	0.77	0	0.77	0	0

(b)

Figure 5.5: Field distributions in two different inhomogeneous, lossy, and layered cylindrical structures.

5.1.3 Thickness variation

We have showed the results of the field distributions in a homogeneous and inhomogeneous cylindrical structure with and without lossy dielectric materials. What also was shown was what kind of impact or influence certain material properties had on the field distribution or its magnitude. Another parameter we can experiment with is the thickness or the radius of certain

layers in the cylindrical structure. In the examples shown in Figures 5.6 and 5.7, the thickness of the second layer (L_2) and the third layer (L_3) is varied respectively. If these examples are to be imagined to a more practical usage which in our case would be an MRI dielectric resonator coil, then the second layer (L_2) could be imagined as the air-gap between the patient and the inner boundary of the dielectric resonator coil. The third layer (L_3) could be imagined as the high permittivity dielectrics inside the resonator coil. If we do not change the thickness of the high permittivity ($\varepsilon_{\mathrm{r}} = 200$) layer of L_3, we can determine that in that particular case the thickness of the second layer ("air-gap") has less influence on the field distributions than changing the thickness of the third layer (high permittivity dielectrics) while keeping the thickness of the "air-gap" layer constant. This can be concluded by comparing Figures 5.7 and 5.6 with each other.

We have simulated multiple cylindrical set-ups ranging from lossless homogeneous dielectrics to lossy inhomogeneous dielectrics. We have shown that there are no discontinuities present at source-free interfaces. What also can be observed is that when there is an electric-current source present at an interface that the magnitude of the discontinuity is equal to the magnitude of the electric current source. Now that we have shown that the analytical model functions correctly we can move on to describe how this analytical tool can be used to help design a more efficient dielectric resonator.

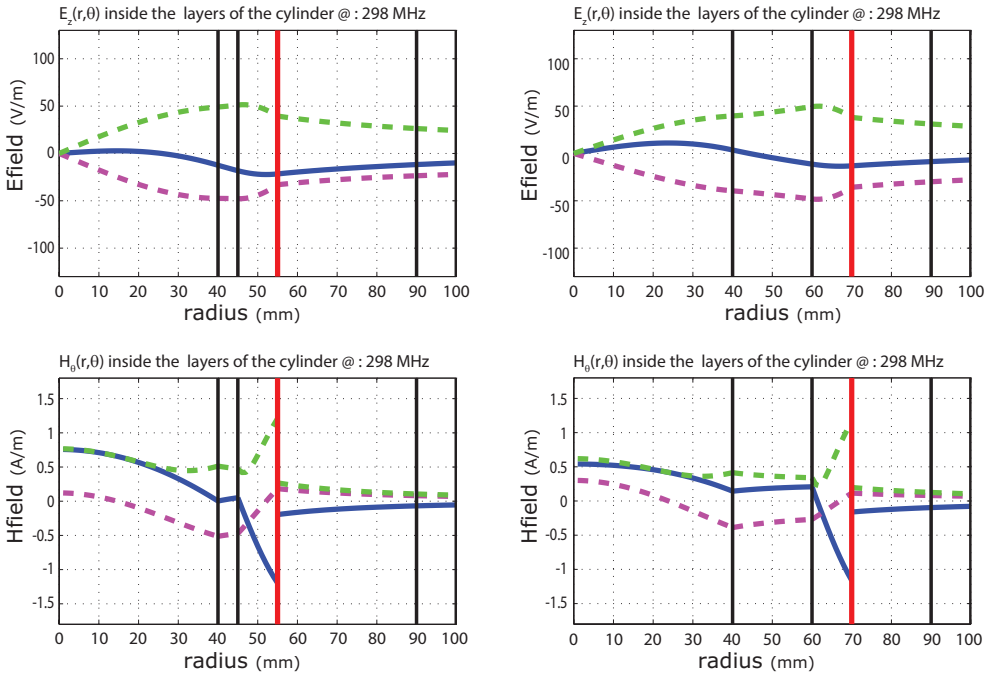

Source J^{amp} = 1 A/m @298 MHz

	L_1	L_2	L_3	L_4	L_5
rad (mm)	40	45	55	90	100
ε_r	50	1	200	1	1
μ_r	1	1	1	1	1
σ	0.77	0	0.1	0	0

(a)

Source J^{amp} = 1 A/m @298 MHz

	L_1	L_2	L_3	L_4	L_5
rad (mm)	40	60	70	90	100
ε_r	50	1	200	1	1
μ_r	1	1	1	1	1
σ	0.77	0	0.1	0	0

(b)

Figure 5.6: (a) Air-gap thickness of 5mm, (b) air-gap thickness of 20mm.

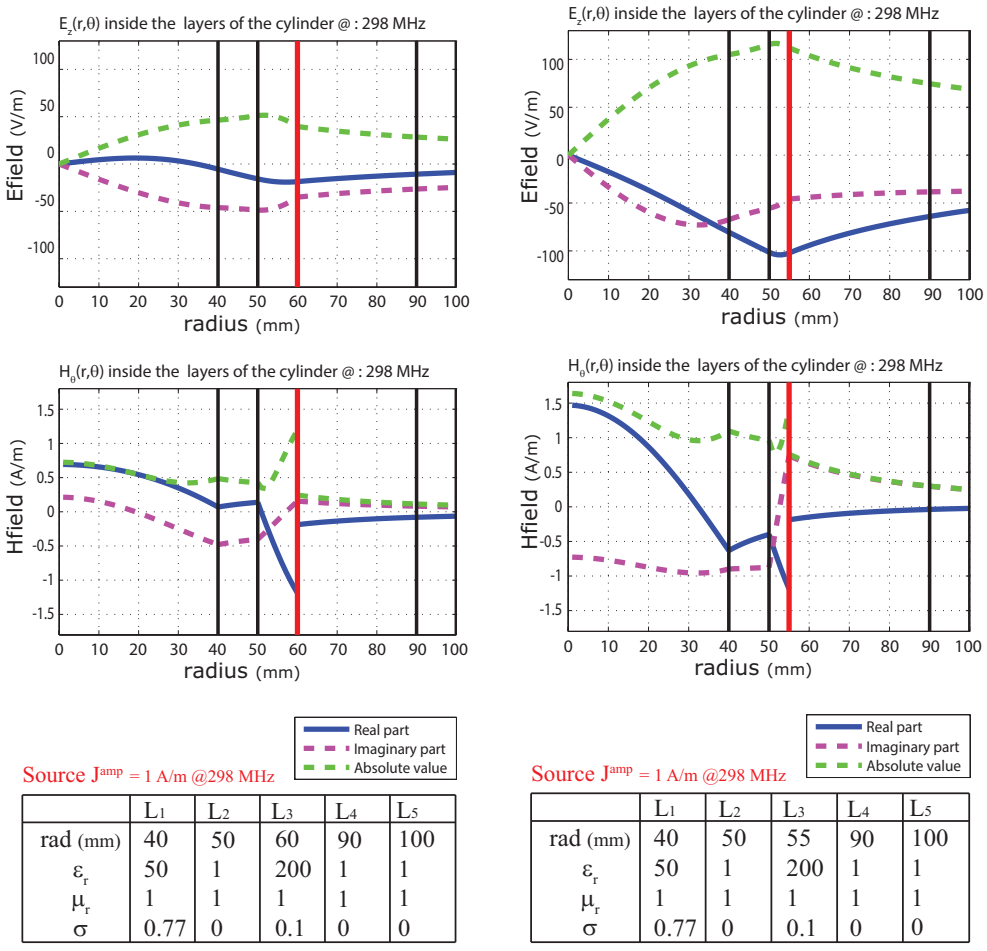

	L_1	L_2	L_3	L_4	L_5
rad (mm)	40	50	60	90	100
ε_r	50	1	200	1	1
μ_r	1	1	1	1	1
σ	0.77	0	0.1	0	0

(a)

	L_1	L_2	L_3	L_4	L_5
rad (mm)	40	50	55	90	100
ε_r	50	1	200	1	1
μ_r	1	1	1	1	1
σ	0.77	0	0.1	0	0

(b)

Figure 5.7: (a) Dielectric-pad thickness of 10mm, (b) dielectric-pad thickness of 5mm.

5.2 Comparing CST with Matlab

There are multiple software suites like XFdtd EM Simulation Software from Remcom and CST's microwave studio that can calculate field distributions numerically. In order to have some form of validation, a comparison will

be made between the eigenmode solver from CST and the analytical tool programmed with Matlab. The simulation setup in CST will involve a cylindrical layered structure consisting of 4 dielectric layers. This cylindrical structure has a finite height (z). This cylindrical structure is illustrated in Figure 5.8a.

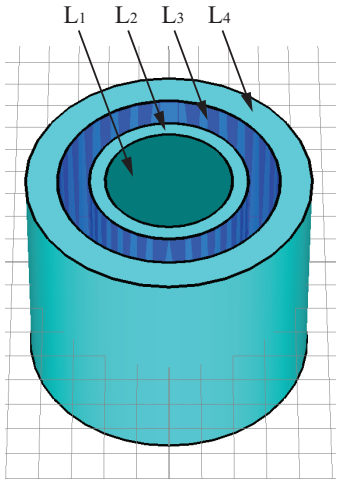

	L_1	L_2	L_3	L_4
rad (mm)	40	50	70	100
ε_r	50	1	80	1
μ_r	1	1	1	1
σ	0	0	0	0

(a)

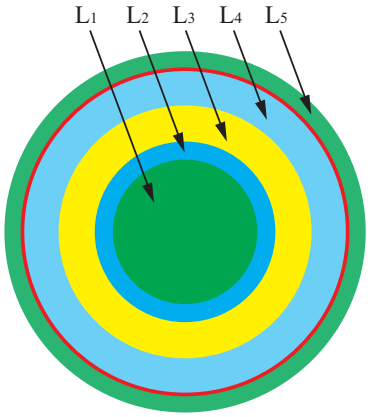

Source

	L_1	L_2	L_3	L_4	L_5
rad (mm)	40	50	70	90	100
ε_r	50	1	80	1	1
μ_r	1	1	1	1	1
σ	0	0	0	0	0

(b)

Figure 5.8: (a) 3D test setup in CST, (b) z-invariant test setup in Matlab.

The cylindrical setup created in CST differs a bit from the one used in the analytical tool. In order to analytically calculate the field distribution with the Matlab tool, a source has to be included into the simulation. Without an added energy source there is no field present inside the dielectric structure. In our case this is the electric-current source (J_z) that we have discussed earlier. The eigenmode solver from CST calculates all the eigenmodes that are theoretically possible to resonate inside the cylindrical structure. It is only possible to carry out these calculations if there is no source present in the cylindrical structure. This is due to the manner the solver calculates the eigenmodes. One of the downsides of this type of solver is that it is generally

not known what the desired mode number will be. Once the calculations are finished we can begin to analyse all the calculated eigenmodes. We need to find the desired resonating field pattern which in our case has the same field pattern as the $HEM_{11\delta}$ mode. The frequency at which this mode is found depends on the permittivity of the materials and the dimensions of the cylindrical structure. It is also a possibility that the desired eigenmode is not found inside the cylindrical structure. It is still possible to get the desired eigenmode by changing the permittivity or the dimensions of the cylindrical structure and run the eigenmode solver again.

As mentioned before, all of the results have to be individually analysed in order to find the desired resonant eigenmode. In these examples we choose to calculate the first 10 eigenmodes as the most dominant eigenmodes tend to be in the first few calculated modes. In our specific MRI related case where the B_0 is parallel to our z-direction, the desired mode is the $HEM_{11\delta}$ mode. We simulate the cylindrical structure shown in Figure 5.8a and give it a height of $z = 152$ mm. When the cylinder has this height and after we analyse the results from the eigenmode solver we see that in this particular case the desired mode is the second one that the eigenmode solver has calculated. The vector plots of the calculated electric and magnetic fields of this desired mode are shown in Figures 5.9a and 5.9b.

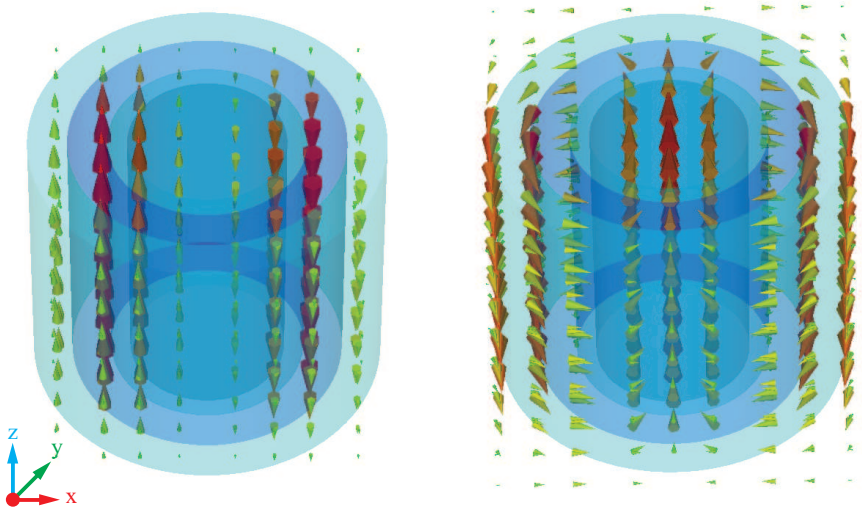

(a) E-field (b) H-field

Figure 5.9: E-field (a) and H-field (b) of the 2nd mode as calculated by the CST eigenmode solver at 263.3 MHz.

After the completion of the CST simulation the results are further evaluated along a line on the x-axis with its origin at half of the height of the cylindrical structure (see Figure 5.10). The result of this evaluation together with an overlay of a simulation with the Matlab programis presented in Figure 5.11 for the electric field and Figure 5.12 for the magnetic field.

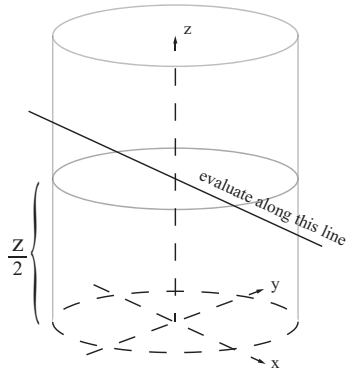

Figure 5.10: The line along which the fields are to be evaluated.

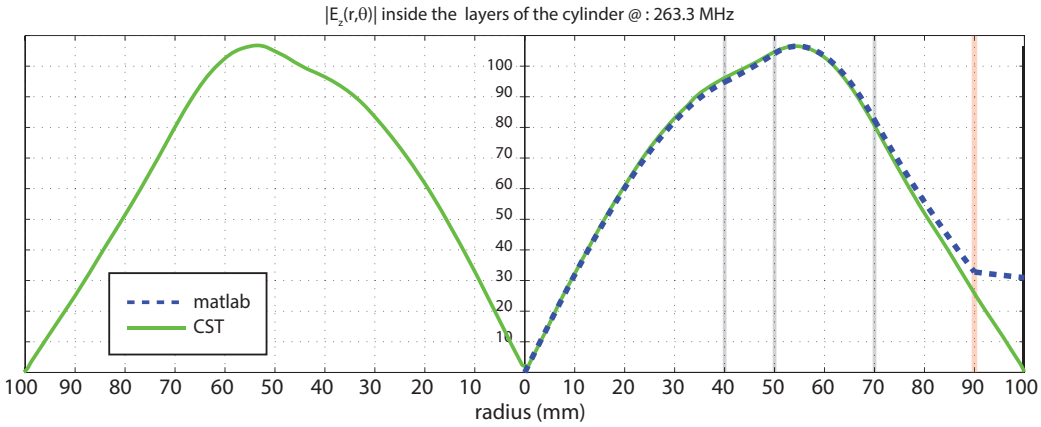

Figure 5.11: Normalized results of the CST eigenmode solver and Matlab simulation results for the electric field.

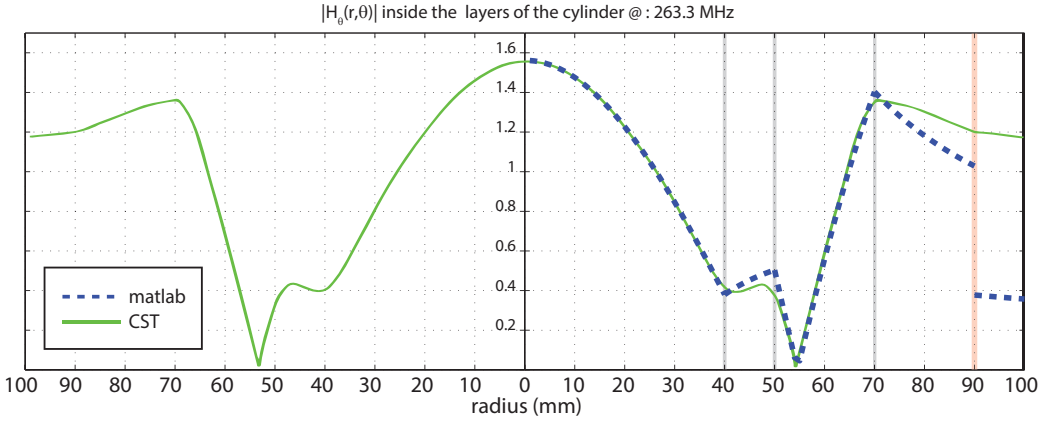

Figure 5.12: Normalized results of the CST eigenmode solver and Matlab simulation results for the magnetic field.

The simulated cylindrical structure in CST and Matlab completely overlap except for the excitation source between the fourth and fifth layer.

The amplitude of the used excitation source in this particular simulation is the same as in the previous examples in this chapter with the exception that its frequency is equal to 263.3 MHz instead of 298 MHz. This is done because at this frequency the eigenmode solver in CST software found this particular resonating mode. The CST results are normalized to the results

of the Matlab program in order to make the similarities between the two different results more visually clear. This example shows that the created Matlab program calculated almost the same field distributions as a widely used and accepted electromagnetic simulation program like CST's microwave studio. The time needed for the CST simulations to complete on the fastest available computer at the Gorter centre (nicknamed "the Beast") was about 3 to 4 hours. This computer has 24 Intel Xeon X5660 cores @2.80 MHz and about 48 GB of internal memory. The Matlab program running on an average desktop computer needs less than 1 second to complete its calculations. The needed simulation time for the Matlab program to complete does not depend on the permittivity used in the cylindrical structure. The eigenmode solver in CST's microwave studio is a numerical solver that discriminates the cylindrical structure according to its electrical size; this depends on its actual size and the permittivity of the materials in the object. Increasing the size of the object or the permittivity will also significantly increase the time for the simulation to complete.

5.3 Set 2: Comparing cylindrical structures of finite and infinite length

As was mentioned previously, the created Matlab model assumes a z-invariant cylindrical structure but of course in reality this is not the case. In order to check if field distributions in the z-invariant model are comparable to a finite cylindrical model, a simulation is done with CST's eigenmode solver. We use the same cylindrical set-up as in Figure 5.8a, but now for each separate simulation we increase the height of the cylinder. The height of the original cylinder was 152 mm which is the same height as the water-based resonator coil that S.A. Aussenhofer *et al.* used in their paper [6]. In each separate simulation we now increase the length of the cylinder by 152 mm until the cylinder has reached a height of 1520 mm.

The field distributions obtained in this way initially remain the same up until a point where the cylinder has reached a height of 608 mm. When we increased the height of the cylinder to 760 mm it was no longer possible to detect any coherent mode structure in the results of the eigenmode solver; this can be seen in Figure 5.13. What also was found is that the desired

mode structure was always found at the same frequency, which in this example was at 262.3 MHz. The corresponding mode number increased when we increased the height of the cylinder. For instance at a height of $z = 152$ mm the desired mode structure was the 2nd mode that the eigenmode solver found. That same mode structure is the 8th mode found in a cylinder with a height $z = 608$ mm, this is also illustrated in Figure 5.13. All these illustrated modes have a z-invariant magnetic field distribution which is a desired feature in magnetic resonance imaging. The magnitude of this magnetic field distribution is shown in Figure 5.16.

We also studied if the same would apply to a homogeneous cylindrical structure. We simulated a homogeneous cylindrically layered structure with an $\varepsilon_{\mathrm{r}} = 4$ and another cylinder with an $\varepsilon_{\mathrm{r}} = 49$. The CST results show that the desired mode structure could at least be supported even when the cylinders height was increased to 1362 mm. The resulting 3D vector plots and the magnetic field distribution of the cylinder with $\varepsilon_{\mathrm{r}} = 4$ and $\varepsilon_{\mathrm{r}} = 49$ can be seen in Figures 5.14 and 5.15, respectively. The magnitude of the magnetic field distribution of these two homogeneous cylindrical structures is shown in Figures 5.17 and 5.18 respectively.

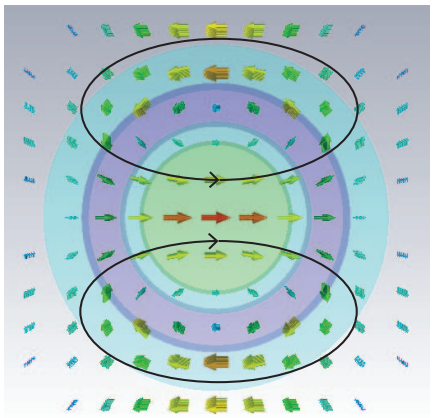

(a) H_θ @ z_1=152mm, 262.3 MHz

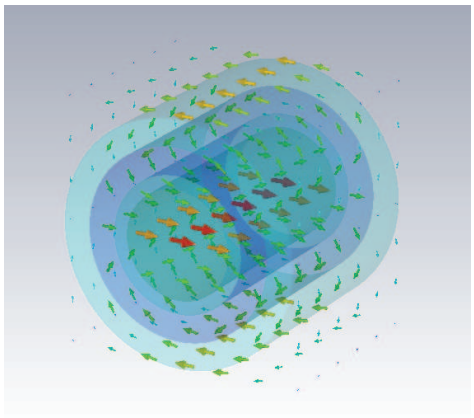

(b) H_θ @ z_1=152mm, 262.3 MHz

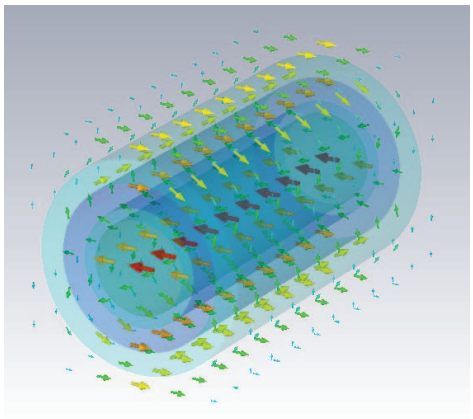

(c) H_θ @ z_2=304mm, 262.3 MHz

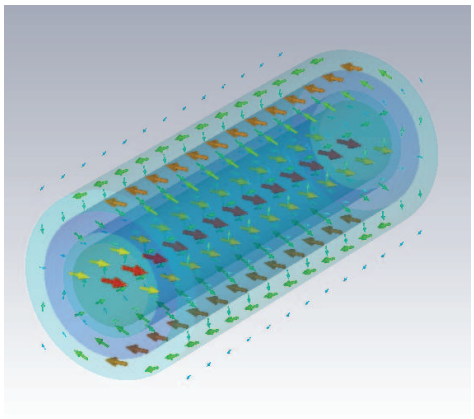

(d) H_θ @ z_3=456mm, 262.3 MHz

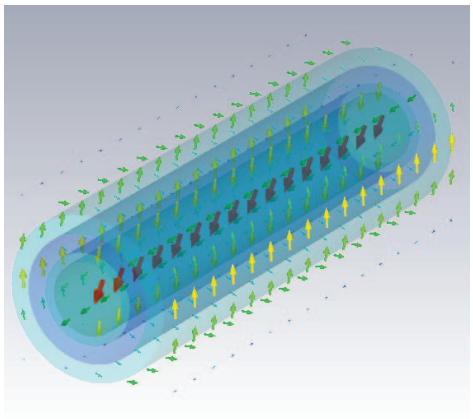

(e) H_θ @ z_4=608mm, 262.3 MHz

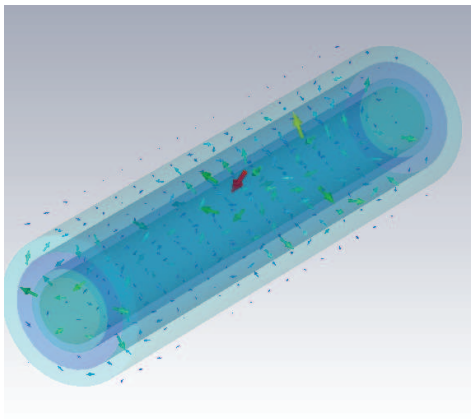

(f) H_θ @ z_5=760mm, 288.1 MHz

Figure 5.13: (a) A planar view of H_θ, (b) – (f) a perspective view of the H_θ field distribution in an inhomogeneous cylinder, where the relative permittivity in the layers are respectively $\varepsilon_{r;1} = 49$, $\varepsilon_{r;2} = 1$, $\varepsilon_{r;3} = 80$, and $\varepsilon_{r;4} = 1$.

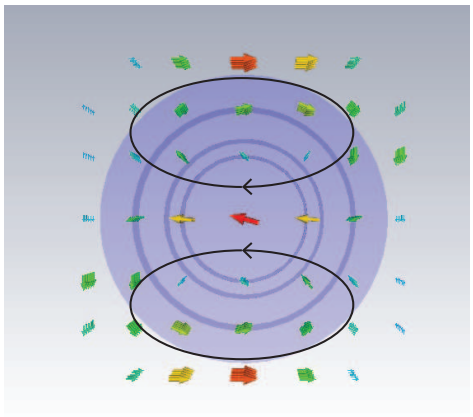

(a) H_θ @ z_1=152mm, mode nr:5

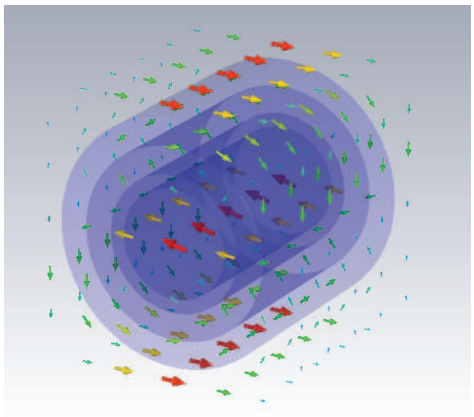

(b) H_θ @ z_1=152mm, mode nr:5

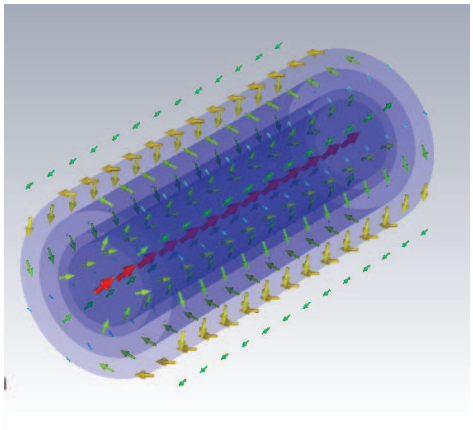

(c) H_θ @ z_2=304mm, mode nr:16

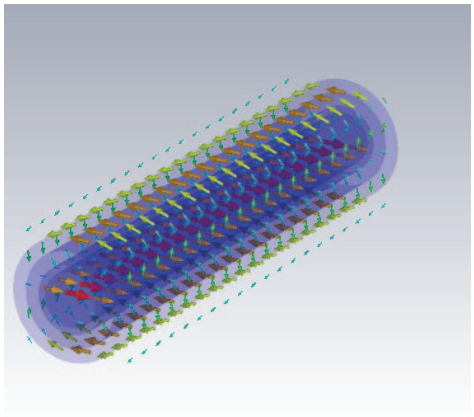

(d) H_θ @ z_3=456mm, mode nr:25

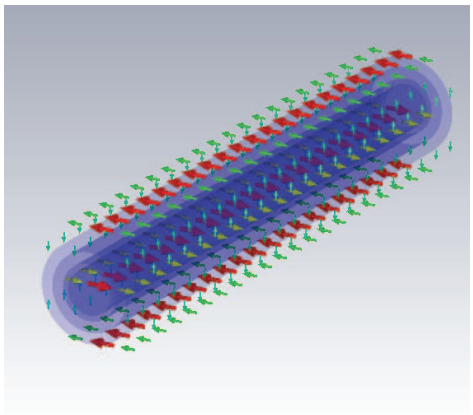

(e) H_θ @ z_4=608mm, mode nr:35

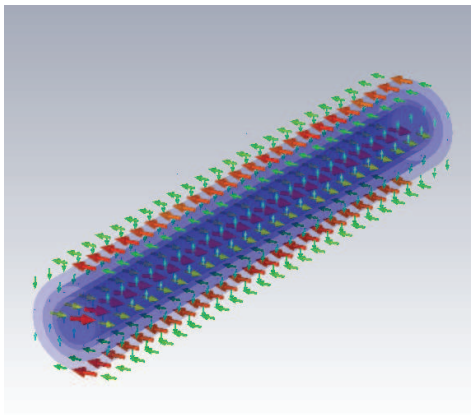

(f) H_θ @ z_5=760mm, mode nr:46

Figure 5.14: (a) A planar view of H_θ, (b)-(f) a perspective view of the H_θ field distribution in the homogeneous cylinder. All layers have a relative permittivity $\varepsilon_r = 4$. All figures the frequency of operation is 853.4 MHz.

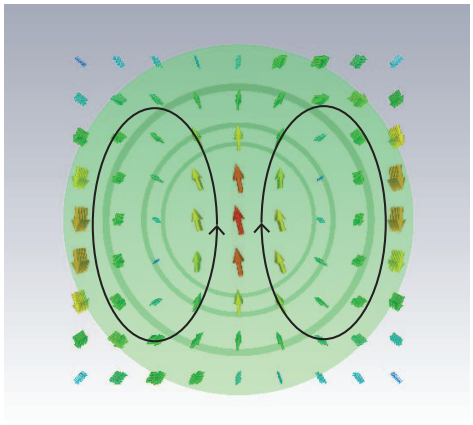

(a) H_θ @ Z_1=152mm, mode nr:4

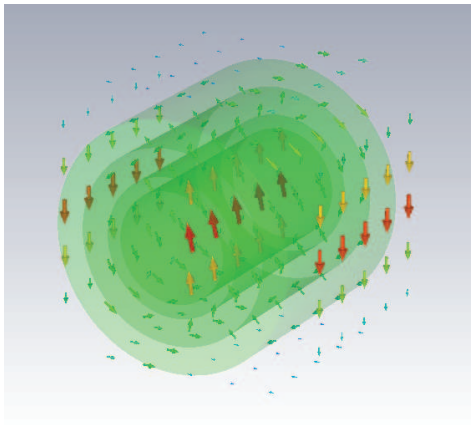

(b) H_θ @ Z_1=152mm, mode nr:4

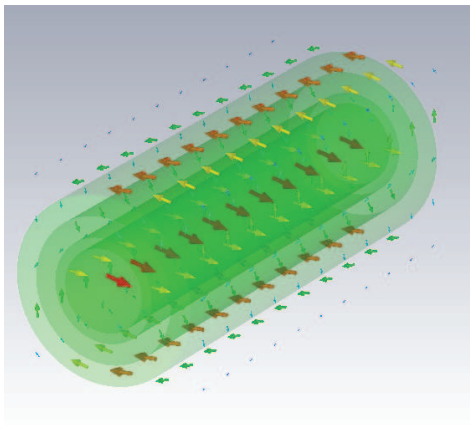

(c) H_θ @ Z_2=304mm, mode nr:10

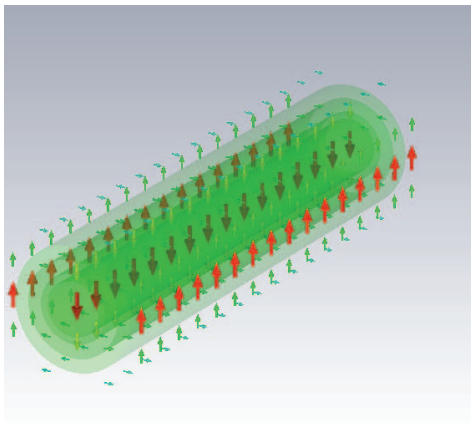

(d) H_θ @ Z_3=456mm, mode nr:18

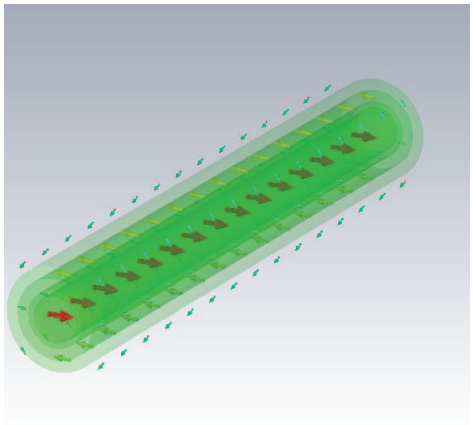

(e) H_θ @ Z_4=608mm, mode nr:23

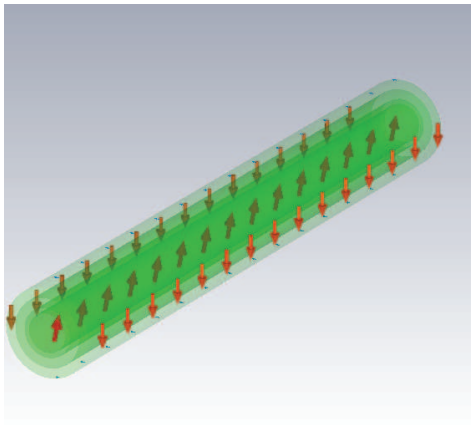

(f) H_θ @ Z_5=760mm, mode nr:49

Figure 5.15: (a) A planar view of H_θ, (b)-(f) a perspective view of the H_θ field distribution in the homogeneous cylinder. All layers have a relative permittivity $\varepsilon_r = 49$. In all figures the frequency of operation is 246.3 MHz.

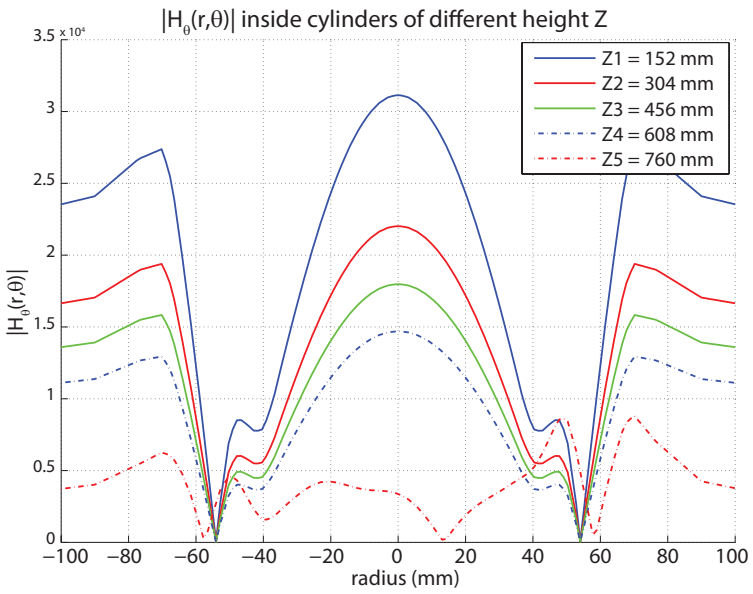

Figure 5.16: $|H_\theta|$ on the measurement line inside an inhomogeneous cylinder, $\varepsilon_{\mathrm{r};1} = 49$, $\varepsilon_{\mathrm{r};2} = 1$, $\varepsilon_{\mathrm{r};3} = 80$, $\varepsilon_{\mathrm{r};4} = 1$.

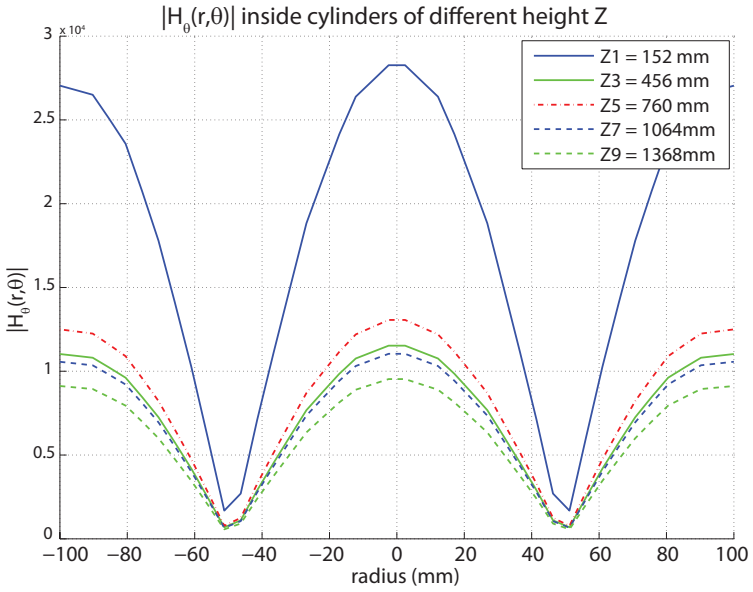

Figure 5.17: $|H_\theta|$ on the measurement line inside a homogeneous cylinder, all layers have a relative permittivity $\varepsilon_{\mathrm{r}} = 4$.

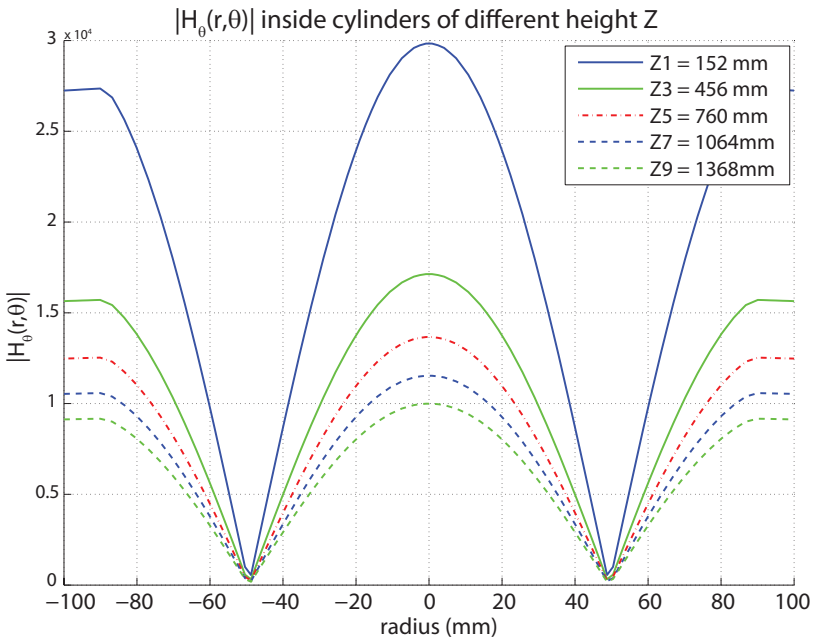

Figure 5.18: $|H_\theta|$ on the measurement line inside a homogeneous cylinder, all layers have a relative permittivity $\varepsilon_\mathrm{r} = 49$.

Notice that the lines in the graph in Figure 5.18 are much smoother than the lines in the graph of Figure 5.17. This is due to the discretization process of the numerical solver where the size of the Yee cell's is related to the relative permittivity. This discretisation process can create problems at the boundaries between two different layers if the discretization grid is not properly aligned with the contours of the simulated object.

5.4 Set 3: Aiding in the design of a practical dielectric resonator

In this section we take a look at how the analytical tool can aid us in the design of a dielectric resonator for wrist applications. In order to get a well functioning dielectric resonator coil it has to be able to transmit a strong and an as homogeneously as possible B_1^+ field. We now are going to use the analytical tool to help us find the most optimal parameters for the thickness and

permittivity of the dielectric material inside the dielectric resonator.

We create a dielectric resonator configuration similar to the one described by Aussenhofer et al. [6]. This configuration has an inner cylinder of tissue ($\varepsilon_{\mathrm{r}} = 50$) with an outer diameter of 80 mm to simulate the human wrist. In this particular experiment we set the maximum dimension of the most outer layer to be 200 mm (free space).

Since the thickness of a human wrist will vary from person to person so will the air-gap between the wrist and the dielectric resonator. A number of experiments will be done in order to study what the optimum thickness of the air-gap between the wrist and the dielectric resonator will be. The thickness of the air-gap will be varied from 10 mm, 5 mm, 1 mm and finally we simulate what the field distributions are if we have no air-gap (0 mm) between the dielectric resonator and the wrist.

The thickness and the dielectric properties of the dielectric resonator itself will also be varied in order to study the effect this will have on the electromagnetic field distribution. The thickness of the dielectric resonator itself will be varied from 15 mm to 10 mm and finally to 5 mm. The relative permittivity of the dielectric material in the resonator will be varied between $\varepsilon_{\mathrm{r}} = 80$, $\varepsilon_{\mathrm{r}} = 150$, and finally $\varepsilon_{\mathrm{r}} = 200$.

In the upcoming figures (Figures 5.19 - 5.22) the air-gap is kept constant at one of the previously mentioned values (10, 5, 1 and 0 mm). In each separate figure the thickness as well as the relative permittivity of the resonator will be varied between the previously mentioned values. The excitation source used in this experiment is the same as in all previous experiments, namely, $J_z^{\mathrm{S}} = J^{\mathrm{amp}} \cos(\theta)$ with $J^{\mathrm{amp}} = 1$ A/m and the frequency of operation is 298 MHz.

If we take a closer look at Figures 5.19 - 5.22, it can be seen that for this specific dielectric resonator setup the simulations where the dielectric resonator itself has a relative permittivity of 150 and a thickness of 5 mm has the highest magnetic field strength inside the tissue layer (inner layer).

We do note, however, that if we change the permittivity or the radius of the tissue layer a totally different conclusion could arise. If we overlay all the graphs involving a dielectric resonator with a 5 mm thickness and a permittivity of $\varepsilon_{\mathrm{r}} = 150$ we can see that the magnetic field strength inside the tissue layer increases if we decrease the air-gap between the simulated wrist

and the dielectric resonator. This overlay is illustrated in Figure 5.23.

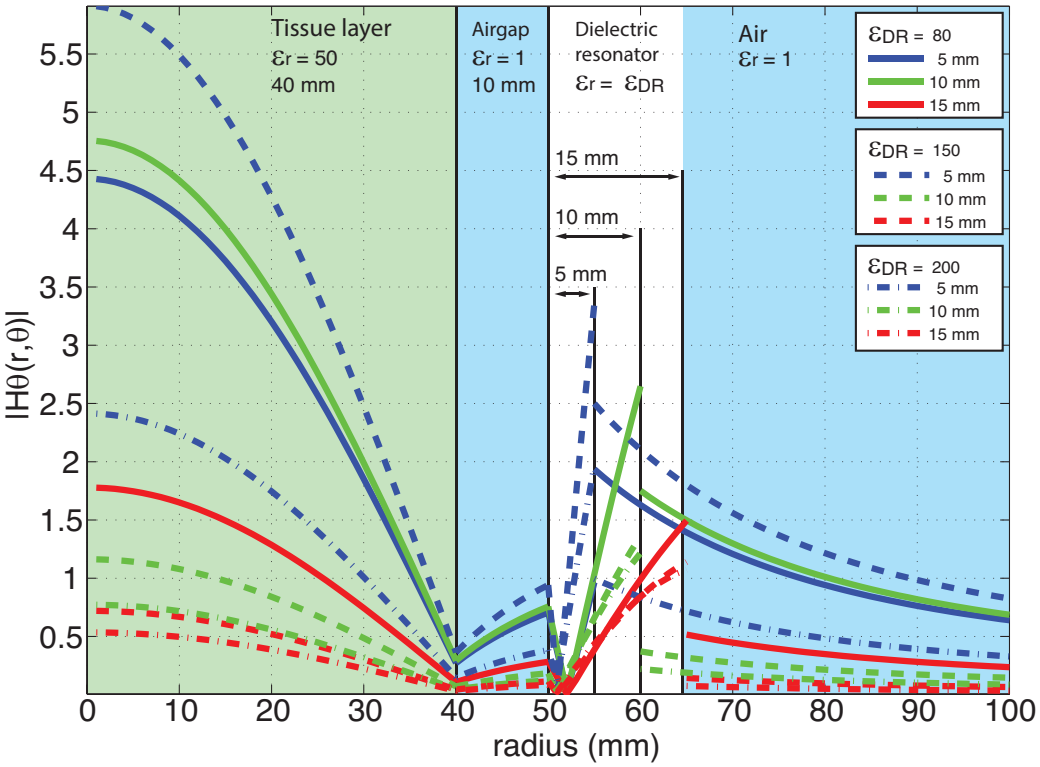

Figure 5.19: Magnitude of the tangential magnetic field strength on the measurement line. The airgap is kept constant at 10 mm, while the permittivity of the dielectric material inside the dielectric resonator varies between 80, 150 and 200. The thickness of the resonator wall is varied between 15, 10 and 5 mm.

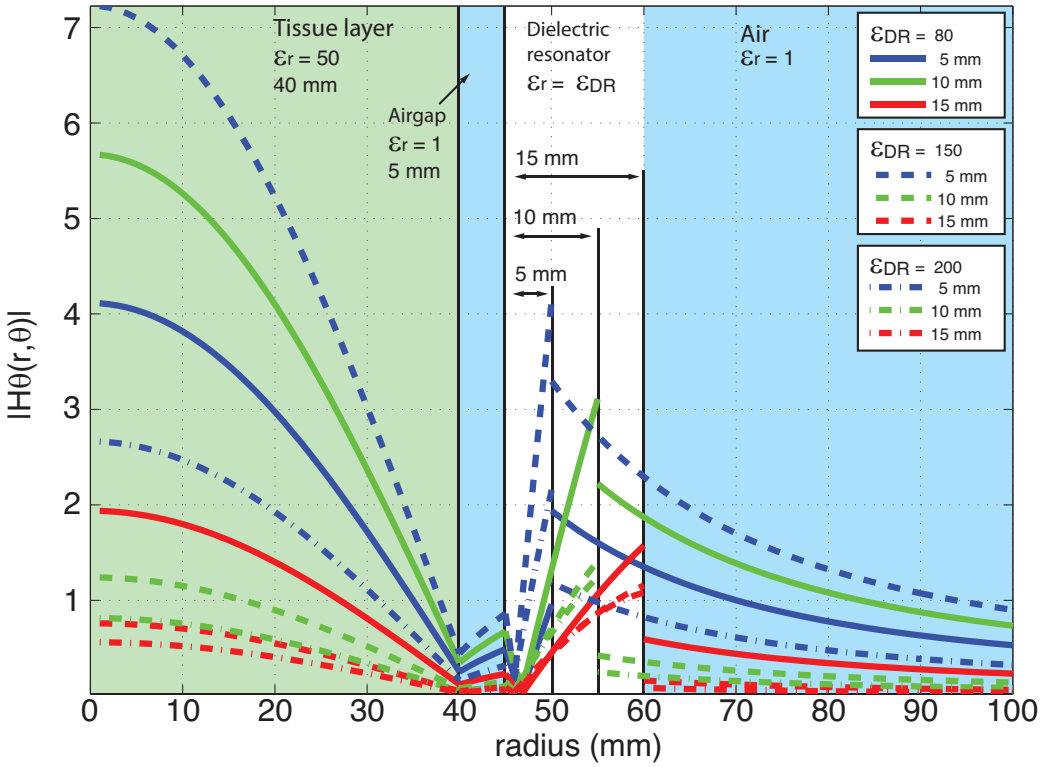

Figure 5.20: Magnitude of the tangential magnetic field strength on the measurement line. The airgap is kept constant at 5 mm, while the permittivity of the dielectric material inside the dielectric resonator varies between 80, 150 and 200. The thickness of the resonator wall is varied between 15, 10 and 5 mm.

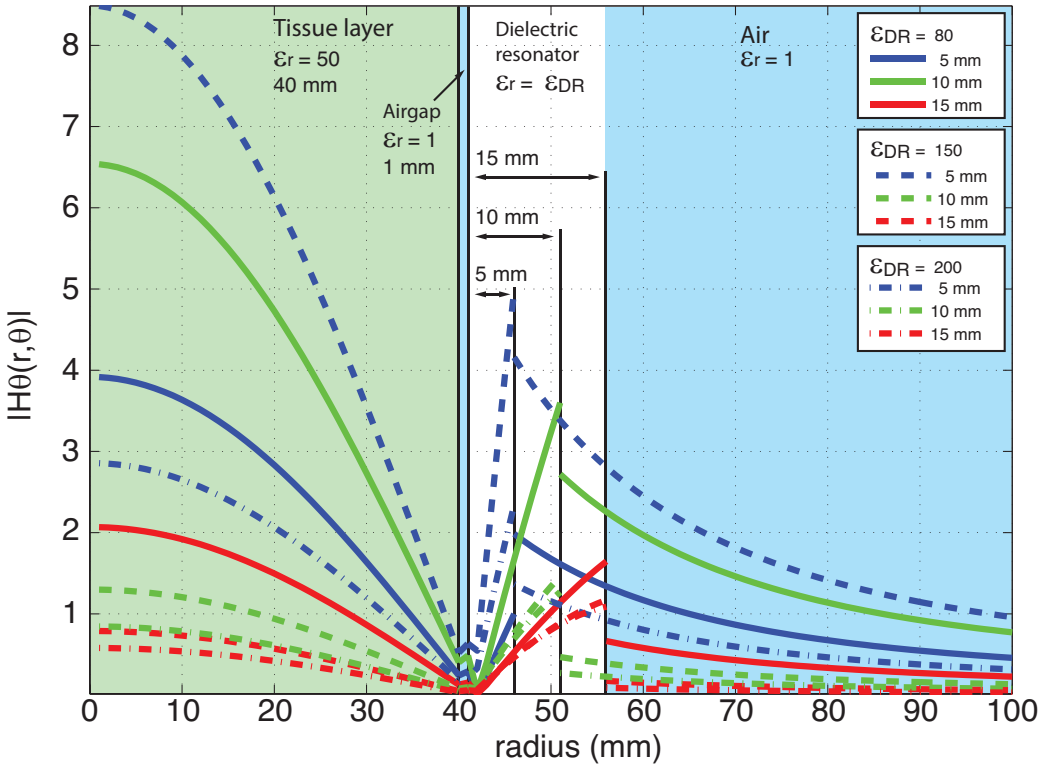

Figure 5.21: Magnitude of the tangential magnetic field strength on the measurement line. The airgap is kept constant at 1 mm, the permittivity of the dielectric material inside the dielectric resonator varies between 80, 150 and 200. The thickness of the resonator wall is varied between 15, 10 and 5 mm.

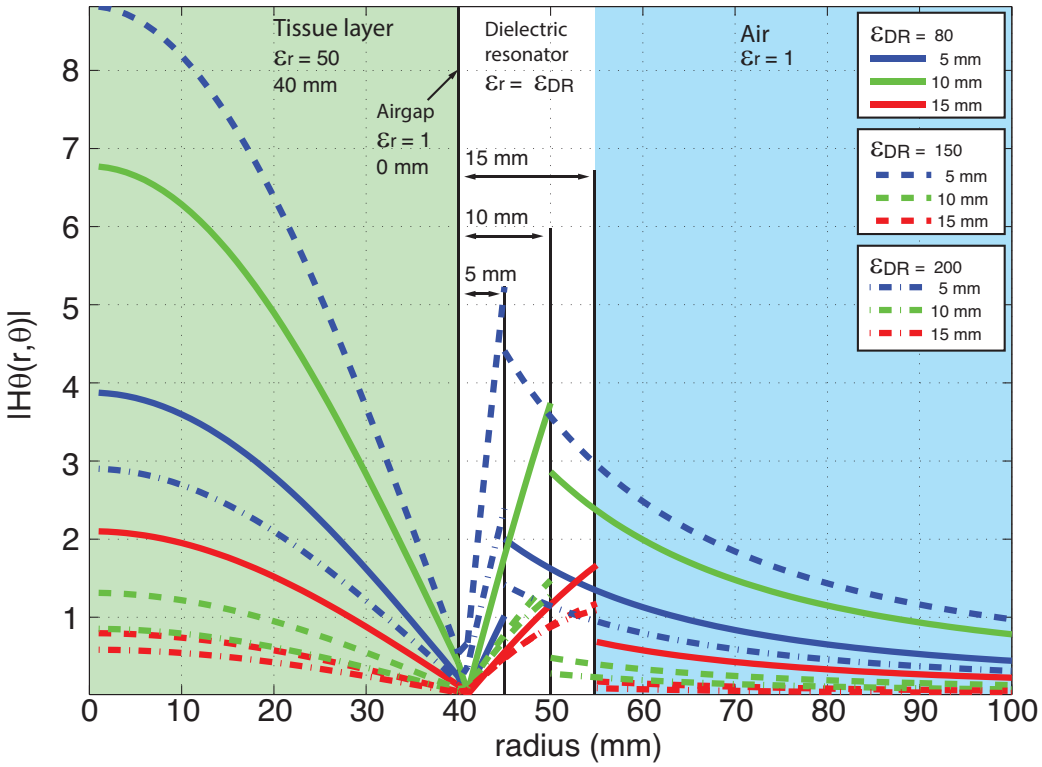

Figure 5.22: Magnitude of the magnetic field strength with no airgap (0 mm) between the tissue layer and the dielectric resonator. The permittivity of the dielectric material inside the dielectric resonator varies between 80, 150 and 200. The thickness of the resonator wall is varied between 15, 10 and 5 mm.

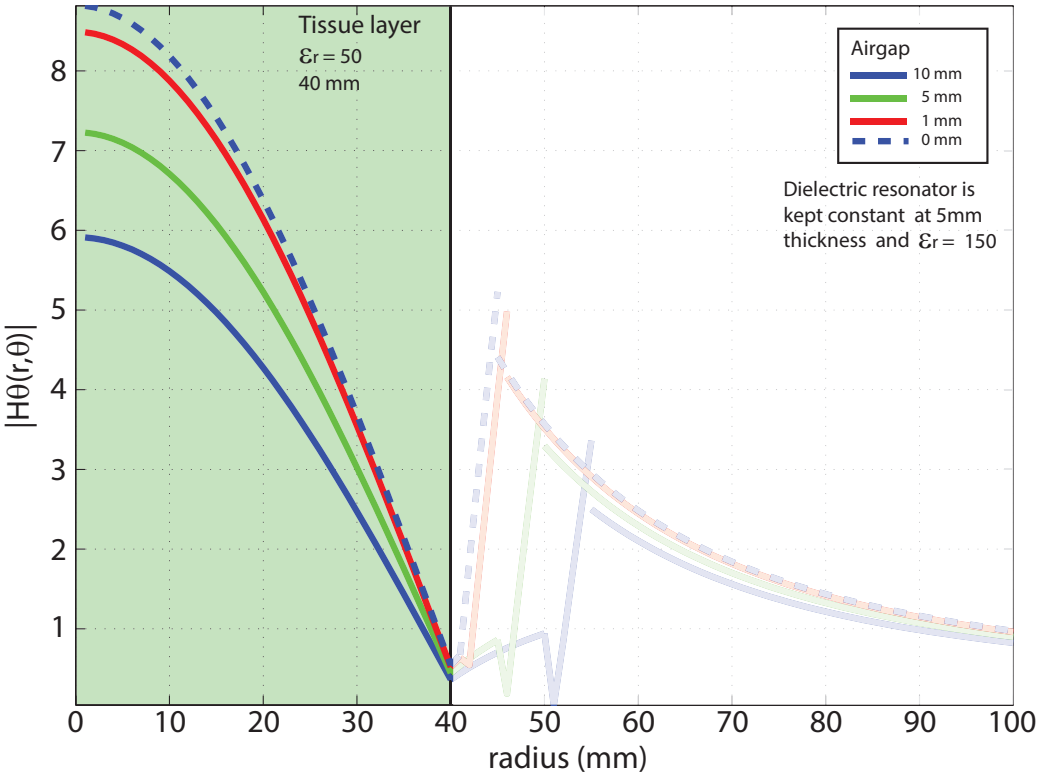

Figure 5.23: Magnetic field distributions inside the tissue layer, parameters of dielectric resonator are kept constant ($\varepsilon_r = 150$, 5 mm thickness) the airgap between the tissue layer and the dielectric resonator is varied between 0 mm, 1 mm, 5 mm and 10 mm.

This example shows that we can use this analytical tool to aid us in designing a dielectric resonator if some upper and lower boundaries are set to its dimensions. This tool also gives us more insight on how field distributions will change if we alter one or more parameters in the simulated cylindrical configuration.

5.5 Getting the B_1^+ field out of the Matlab program

In the previous section we focused on determining the E-field and the H-field but in practice MR researchers and engineers tend to be more interested in the B_1^+ field. As was mentioned in chapter 2.2, the B_1^+ field is commonly used for determining the homogeneity of the transmitted magnetic field. Both the eigenmode solver in CST and the created Matlab program calculate the electromagnetic field components in its real and imaginary parts. The homogeneous transmitted B_1^+ field can be calculated by using

$$B_1^+ = \frac{B_x + iB_y}{2} = \mu_0 \frac{H_x + iH_y}{2}. \tag{5.5.1}$$

The B_1^+ field is made up from the real and imaginary components perpendicular to the main B_0 field. For the x- and y-components of the magnetic field strength we have

$$H_x = \cos(\theta)H_r - \sin(\theta)H_\theta \tag{5.5.2}$$

and

$$H_y = \sin(\theta)H_r + \cos(\theta)H_\theta \tag{5.5.3}$$

Substitution leads to

$$|B_1^+| = \frac{\mu_0}{2}|H_r + iH_\theta|, \tag{5.5.4}$$

where we have used Euler's formula $e^{i\theta} = \cos(\theta) + i\sin(\theta)$.

In order to incorporate the possibility to determine the B_1^+ field some additional code is required in the Matlab program. More specific the code that needs to be added has to calculate the $H_r(r, \theta)$ field. The equation described in Eq. (4.2.8) can be used to calculate this particular magnetic field part.

Chapter 6

Discussion and Conclusion

In order to get high quality MR images, the transmitted magnetic field (B_1^+) has to be as homogeneous as possible. In order to design and construct volume coils that are capable of creating such homogeneous B_1^+ fields, we first need to get insight in the magnetic field distribution inside the to be constructed volume coil. Generally, this is achieved by running multiple numerical simulations prior to the construction of the volume coil. These simulations require large amounts of computational resources and time to complete. These time consuming simulations prohibit a fast insight and understanding on what will change in the field distribution if one of the parameters is slightly changed. For example, the air-gap between the coil and a moving patient. An analytical calculation tool could determine these field distributions much faster. A drawback of this tool is that the analytical model only determines the field distributions of z-invariant cylindrically layered structures.

In the examples of the previous chapter we showed that the results of the analytical tool were almost identical to that of the numerical eigenmode solver of CST. These illustrations show that the shape and trend of the electromagnetic field distribution stays the same when the height of the cylindrical structure is increased or decreased. Only the magnitude of the fields will change. This is a strong indication that the constructed analytical tool not only can be used for determining the field distributions in z-invariant cylindrical structures but also in cylindrical structures with a finite height. Still the field distributions at the edges of the cylinder e.g. the top and bottom

cannot be accurately determined with this analytical model.

Further study on the validity of this analytical model could be done by creating a phantom which consists of multiple cylindrical layers filled with different dielectric material. A comparison between the B_1^+ field from an actual MRI scan and an analytically determined B_1^+ field would be desirable. Improving the Matlab code to include a more user friendly interface with the possibility to do parameter sweep simulations would also be beneficial. In this thesis project we desired that the $\mathrm{HEM}_{11\theta}$ mode was the only mode excited in the dielectric resonator. This resulted in a harmonic cosine source $J_z^{\mathrm{S}}(\theta) = J^{\mathrm{amp}} \cos(\theta)$. This is currently the only type of source that is coded in the analytical tool. The Matlab code needs to be augmented if other modes and excitation sources are to be simulated.

To conclude, the tool developed in the MSc project can support MRI coil design by rapidly determining the field distributions inside cylindrically layered structures with dimensions that are generally used in MRI experiments. It is possible to incorporate all of the electromagnetic properties like permittivity, permeability and conductivity in the simulation. The time it takes to complete a simulation is less than one second, this is independent of the electromagnetic properties and the number of layers used in the cylindrical structure. This significant time reduction enables the RF coil engineer to perform multiple simulations in order to get a better understanding and insight on how the fields are distributed and connected to one another.

Bibliography

[1] Lim, B.-T. *Dielectric Resonator Antennas : theory and design*. Ph.D. thesis, Massachusetts Institute of Technology (1999).

[2] Chew, W. C. *Waves and Fields in Inhomogenous Media* (Wiley, 1999).

[3] Balanis, C. A. *Engineering Electromagnetics* (Wiley, 1989).

[4] Jin, J.-M. *Electromagnetic Analysis and Design in Magnetic Resonance Imaging* (CRC Press, 1999).

[5] Hayes, C. E., Edelstein, W. A., Schenck, J. F., Mueller, O. M. & Eash, M. An efficient, highly homogeneous radiofrequency coil for whole-body NMR imaging at 1.5T. *Journal of Magnetic Resonance (1969)* **63**, 622–628 (1985).

[6] Aussenhofer, S. A. & Webb, A. G. Design and evaluation of a detunable water-based quadrature HEM11 mode dielectric resonator as a new type of volume coil for high field MRI. *Magnetic Resonance in Medicine* **68**, 1325–1331 (2012).

[7] Kajfez, D., Glisson, A. & James, J. Computed modal field distributions for isolated dielectric resonators. *IEEE Transactions on Microwave Theory and Techniques* **32**, 1609–1616 (1984).

[8] Webb, A. Visualization and characterization of pure and coupled modes in water-based dielectric resonators on a human 7T scanner. *Journal of Magnetic Resonance* **216**, 107–113 (2012).

[9] Webb, A. Dielectric materials in magnetic resonance. *Concepts in Magnetic Resonance Part A* **38A**, 148–184 (2011).

[10] Abramowitz, M. & Stegun, I. A. *Handbook of Mathematical Functions: With Formulas, Graphs, and Mathematical Tables* (Courier Dover Publications, 1964).

[11] de Heer, P., Brink, W., Kooij, B. & Webb, A. Increasing signal homogeneity and image quality in abdominal imaging at 3T with very high permittivity materials. *Magnetic Resonance in Medicine* **68**, 1317–1324 (2012).

[12] Smith, N. B. & Webb, A. *Introduction to Medical Imaging Physics, Engineering and Clinical Applications* (Cambridge University Press, Cambridge, 2010).

[13] Kajfez, D. *Dielectric resonators* (Noble Pub. Corp., Tucker, Ga., 1998).

[14] Whites, K. W. Electromagnetic wave propagation through circular waveguides containing radially inhomogeneous lossy media. Tech. Rep., AA(Army Construction Engineering Research Lab., Champaign, IL.) (1989).